JOURNAL OF GEOPHYSICAL RESEARCH: PLANETS, VOL. 118, 1365–1387, doi:10.1002/jgre.20081, 2013

Hydrology of early Mars: Valley network incision

Yo Matsubara,[1] Alan D. Howard,[1] and J. Parker Gochenour[2]

Received 24 September 2012; revised 6 February 2013; accepted 16 April 2013; published 28 June 2013.

[1] Widespread occurrences of valley networks on Mars provide geomorphic evidence for an active hydrologic cycle. To constrain the climatic conditions capable of forming the valley networks, a hydrological model was used to analyze the valley incision depth and volume of eroded valleys. Because the absolute magnitudes of precipitation, runoff, and evaporation are uncertain, we have used the ratio of these quantities (the *X-ratio*) to express climatic conditions. The spatial distribution and strength of the correlations between (1) the estimated depth and volume of eroded material and (2) estimated flood magnitude and valley gradients were investigated as a function of the assumed *X-ratio*. We also conducted an analysis of conditions required to have appreciable discharge in selected valley networks, which provided the most definitive constraint on Martian paleoclimate. The other methods show a relatively weak dependency of incision depths and volumes upon the assumed *X-ratio*. The multiple regression analyses indicate that incision depth is strongly influenced by gradient and weakly related to modeled flood discharge. The factors determining relative depth of incision depend partly on the type of channel bed. However, postflow modification of the valley networks by mass wasting, cratering, aeolian infilling, and ice-related processes precludes direct determination of bed morphology. Our hydrological analyses suggest that climatic conditions on early Mars were at least as moist as those that occurred in the Great Basin region of the U.S. when large lakes were present during the Pleistocene in terms of the balance of runoff and lake evaporation.

Citation: Matsubara, Y., A. D. Howard, and J. P. Gochenour (2013), Hydrology of early Mars: Valley network incision, *J. Geophys. Res. Planets*, *118*, 1365–1387, doi:10.1002/jgre.20081.

1. Introduction

[2] To date, simulations of early Martian climate have been unable to reproduce conditions conducive to an active hydrologic cycle, due to the composition of the primordial atmosphere, ease of escape of volatiles as a consequence of the lower Martian gravity and the early loss of the magnetic field, and the lower luminosity of the early Sun [e.g., *Feulner*, 2012; *Wordsworth et al*., 2011]. Energy additions from large impacts and short-term enhancement of greenhouse gasses from volcanism have been suggested as causes of short-duration warmer periods [e.g., *Feulner*, 2012; *Segura et al*., 2012].

[3] Despite uncertainties surrounding the atmospheric conditions of early Mars, fluvial landforms in the southern highlands provide geologic evidence for a climate capable of sustaining an active hydrological cycle [*Burr et al*., 2009; *Hynek and Phillips*, 2003; *Irwin et al*., 2005a, 2005b; *Malin and Edgett*, 2003; *Moore et al*., 2003; *Moore and Howard*, 2005]. Valley networks incised up to several hundred meters into the cratered highlands are ubiquitous on the equatorial cratered highlands on Mars, and the widespread occurrence of such networks demonstrates that flow capable of bedrock erosion and sediment transport occurred in the past. The broad areal distribution of these networks also indicates that these fluvial flows were dominantly driven by runoff resulting from precipitation [e.g., *Carr*, 2012; *Craddock and Howard*, 2002; *Grant*, 2000; *Hynek and Phillips*, 2001, 2003; *Irwin et al*., 2008].

[4] In our previous study, we have used the hydraulic routing model and breached crater rim elevation to constrain the possible ratio of precipitation, runoff, and evaporation (expressed as *X-ratio*, discussed in section 2) required to have overflow from these crater basins [*Matsubara et al*., 2011]. To further our understanding of the early Martian climate, this study utilizes a hydraulic routing model to constrain the ratio of precipitation, runoff, and evaporation that best accounts for the fluvial incision that formed the valley networks. Our approach is similar to examinations of downstream hydraulic geometry in terrestrial fluvial networks interrelating spatial variations of fluvial morphology in response to controlling variables [e.g., *Knighton*, 1987; *Leopold and Maddock*, 1953]. Specifically, the depth of valley incision and the cumulative volume of eroded valleys within Martian drainage networks are related to estimated relative discharges and valley gradients.

[5] The overall objective of this study is to provide additional constraints to the hydrologic environment during valley network formation by finding the relative measure

[1]Department of Environmental Sciences, University of Virginia, Charlottesville, Virginia, USA.
[2]School of Law, University of Virginia, Charlottesville, Virginia, USA.

Corresponding author: Y. Matsubara, Department of Environmental Sciences, University of Virginia, P.O. Box 400123, Charlottesville, VA 22904-4123, USA. (ym9z@virginia.edu)

2169-9097/13/10.1002/jgre.20081

of wetness or aridity (the *X-ratio* discussed below) that result in the best fit for the incision amount, and thus characterize the climate of early Mars.

2. Hydrological Model

[6] Previously, we developed a hydrologic routing model to estimate stream flow and lake distribution on the southern highlands [*Matsubara et al*., 2011]. This model uses Mars Orbiter Laser Altimeter (MOLA) digital elevation models (DEMs) to determine flow direction and balances runoff generated from precipitation and lacustrine evaporation to estimate the distribution of lakes on early Mars and relative flow rates in valley networks. MOLA DEM is in cylindrical projection and we used geographic coordinates to calculate valley length using the equatorial radius. Length in *x*-direction was corrected by Cos(latitude). The model is based on the annual balance of precipitation, runoff, evaporation, and lake area within any enclosed basin

$$V_O = V_I + (A_T - A_L)PR + A_L P - EA_L, \quad (1)$$

where V_O is the yearly volumetric overflow to downstream basins from overflow of the lake, V_I is the inflow from upstream overflowing lakes, A_T is the total area of the enclosed basin (including any lakes/depressions), A_L is the surface area of the lake within the basin, P is the yearly precipitation depth falling on the basin (assumed to be locally uniform), R is the fraction of precipitation falling on unsubmerged uplands that contribute to runoff, and E is yearly evaporation depth from lakes. Water follows the steepest path downslope until it comes to the lowest point of the topography where the flow terminates. As a consequence, the model creates a small lake at every terminus of the channel to keep the hydrology balanced. The size of each lake depends on the climatic condition used for the simulation. In reality, because the flow routing is based on yearly averages of P, R, and E, simulated small lakes may be ephemeral in arid climates as occurs in desert playas. The simulated perennial lake provides the same yearly evaporation as a larger but ephemeral playa lake. For larger lakes relative intra-annual variations in lake size are small.

[7] Because the actual values of precipitation, runoff, and evaporation are uncertain, these parameters are replaced by a single number called the *X-ratio* [*Matsubara et al*., 2011]. The *X-ratio* is a measure of relative climatic aridity, similar to indices used in terrestrial climate studies [*Budyko*, 1974; *Milly*, 1994], and is defined as

$$X = \frac{(E - P)}{RP}. \quad (2)$$

[8] Small *X-ratios* imply humid conditions with little lake evaporation and nearly complete runoff, and large values reflect desert-like settings. The *X-ratio* does not correspond to one exact combination of precipitation, runoff, and evaporation. For example, an *X-ratio* of 4 could result from combinations such as $P = 0.5\ \mathrm{m\ yr^{-1}}$, $R = 0.25$, $E = 1\ \mathrm{m\ yr^{-1}}$ or $P = 1.43\ \mathrm{m\ yr^{-1}}$, $R = 0.1$, $E = 2\ \mathrm{m\ yr^{-1}}$. Nonetheless, whatever the combination of the actual values may be, for an *X-ratio* of 4, the resulting lake size and the connectivity of the drainage networks would be the same. Terrestrial settings with through-flowing drainage generally have *X-ratios* between −1 and zero, and hot deserts such as in the Great Basin region in the southwestern U.S. can experience *X-ratios* exceeding 20. The role of the *X-ratio* in basin hydrology can be illustrated by considering an enclosed basin without inflows or outflows ($V_O = V_I = 0$ in equation (1)), so that the equilibrium size of the lake within the basin relative to the total basin area is a function of the *X-ratio*

$$\frac{A_L}{A_T} = \frac{1}{(X + 1)}. \quad (3)$$

[9] The *X-ratio* is used to define the connectivity of the drainage network by determining which lakes would overflow and extend flow further downstream. For further details of the flow routing procedures and definition of *X-ratio* see *Matsubara and Howard* [2009] and *Matsubara et al*. [2011].

[10] Because large lakes require multiyear changes in this balance to effect appreciable changes in lake levels, we do not include event-based flow routing in determining the active drainage network. Also, because connectivity of the flow depends on the lake overflow, the flow routing procedure is based on yearly balances of runoff and evaporation. However, erosion of channel beds and transport of sediment through fluvial systems primarily occurs during high-flow events that usually happen during a small fraction of the year. To model these larger "effective discharges", we have made several additional assumptions. Because large lake basins typically require tens to hundreds of years to reach a size that is in equilibrium [e.g., *Matsubara and Howard*, 2009; *Matsubara et al*., 2011], we assumed that when individual high-flow events enter large lakes, the total volume of water that is added is much smaller than the total lake volume; hence, it is assumed that individual floods will not cause a lake to overflow if it is not already indicated to be overflowing based on the balance of annual runoff and evaporation. Flood discharges do follow the network defined by the prevailing *X-ratio* but the magnitudes of these flows are assumed to be much greater than the mean annual flow and are calculated as a separate step from the annual flow routing determining drainage network connectivity.

[11] Our default model for flood discharges assumes spatially uniform runoff and no additional evaporative losses during translation of the flood through the drainage network defined by the *X-ratio*.

3. Background and Prospectus

[12] In *Matsubara et al*. [2011], we conducted simulations using 18 different values of the *X-ratio* ranging from −1 to 19. Each simulation assumed uniform precipitation over the Martian surface, and permitted assessment of conditions necessary for overflow of individual lake basins. Based on the inventory of enclosed basins that are thought to have overflowed during the Late Noachian on Mars [*Fassett and Head*, 2008a], we concluded that the corresponding *X-ratios* were in the range of 3 to 7, which roughly corresponds to the evaporation and precipitation regime that characterized the Great Basin region during the late Pleistocene epoch when the lakes Lahontan and Bonneville were at their fullest extent [*Matsubara and Howard*, 2009].

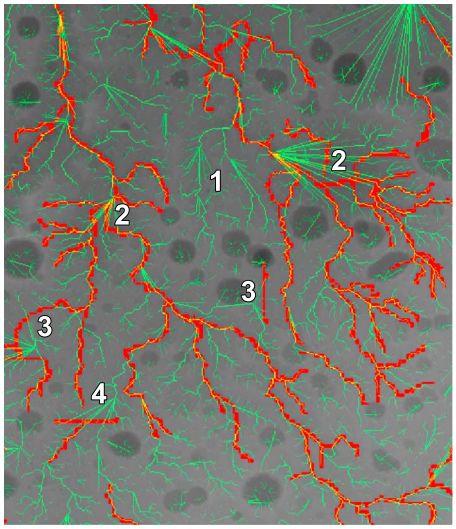

Figure 1. Example of delineated valley networks by hydrological routing model (green/yellow) and mapping (red) for the Samara, Parana, and Loire Valles region (see Figure 7 for location). Valley network for hydrologic routing shown for an *X-ratio* of 2.1. Grey is the MOLA topography. Yellow lines indicate segments of valley network where the two delineation methods matched. Converging straight green lines connect lake inflows to the single outflow. The extent of lakes in hydrological routing varies with the assumed *X-ratio*. In valley mapping channels were generally extended to the center of enclosed basins and connected across depressions where exit breaches occurred. "1" shows a location where tributaries are identified by hydrological routing but were not identified in mapping. Generally, these are very shallowly incised valleys. "2" are areas submerged in hydrological routing for this *X-ratio* but mapped as valleys. "3" is where paths of mapped channels and hydrologically routed channels exhibit large deviations. "4" marks location where valleys mapped as unconnected are connected in hydrological routing. Map width about 765 km, centered at 343.7°E 24.9°S.

[13] A similar analysis can be conducted using the valley incision depth and the volume of the eroded valleys. Because the fluvial systems on Mars generally dissect a recognizable upland surface, we can estimate the depth of incision and excavated valley volumes. The amount of valley network incision over the surface provides constraints on the hydrological conditions of early Mars that are independent of our previous study of lake overflows [*Matsubara et al*., 2011]. The methodology utilized in this paper involves several steps and assumptions beyond those used in the *Matsubara et al*. [2011] study of lake hydrology during the time period of valley network excavation. A brief preview of our approach is provided below:

[14] 1. Valley networks were mapped using two different methods: mapping by the hydrological routing model and the traditional hand mapping. For both methods, a combination of spacecraft images and MOLA topography were used. Hydrologic routing using yearly hydrological balances and MOLA topography provided a map of the simulated drainage network and lake distribution for each assumed value of the *X-ratio*. In most cases the mapped and simulated distribution of valley networks were nearly coincident (Figure 1).

[15] 2. The valley networks are typically sharply incised into an older landscape, itself strongly degraded by fluvial and other processes [e.g., *Carr*, 2012; *Howard et al*., 2005]. We developed a methodology for estimating local values of the depth of valley incision into this older topography and the cross-sectional area of valleys, and downstream cumulative volumes of eroded valleys.

[16] 3. Floods responsible for valley network erosion were calculated as a separate step from the annual flow routing procedures. Flood discharges do follow the network defined by the prevailing *X-ratio* but the magnitude of these flows is assumed to be much greater than the mean annual flow.

[17] 4. We correlate the spatial variations of estimated depth and cumulative volumes of valley erosion with local values of estimated flood magnitude and with local and basin-averaged valley gradients using single or multiple regression models of the form

$$Y = KX_1^{\beta_1}X_2^{\beta_2}, \tag{4}$$

where Y is the response variable such as depth of incision, and the X_i are the predictor variables, such as valley gradient and flood magnitude. We explore the strength of these correlations as a function of the assumed *X-ratio*, how they vary spatially throughout the Martian highlands, and the implications of these for predictive models of expected spatial variation in the depth of valley incision. For additional detail on analysis procedures see Table 1.

4. Methodology

4.1. Model Formulation

[18] We explore two additional hydrologic scenarios to account for possible orographic effects on precipitation and attenuation of floods within overflowing lakes.

4.1.1. Orographic Effects

[19] Precipitation, and hence runoff, are typically controlled by orographic effects, and consequently in mountainous terrain on Earth, precipitation is concentrated at high elevations. Large craters and basin topography on Mars have relief variations similar to mountains on Earth, and it is likely that large craters and basins on Mars experienced similar orographic effects on precipitation under higher atmospheric pressures of early Mars [*Forget et al*., 2013; *Scanlon et al*., 2012]. The morphology of alluvial fans and some valley systems on Mars are consistent with orographic influence on runoff [*Howard and Moore*, 2011; *Moore and Howard*, 2005] with most drainage originating from upstream highlands. To explore the role of orographic effects on precipitation, we conducted hydrological simulations with the local *X-ratio* and flood runoff being a function of relative elevation.

[20] To formulate a relief-dependent hydrological model, we used observations of the elevation dependence of precipitation, runoff, evaporation, and mean annual temperature for the Great Basin region of the southwestern U.S. where enclosed basin topography provides good analogy to Mars [*Matsubara and Howard*, 2009]. Precipitation in this region exhibits relatively strong correlation (correlation coefficient = 0.42) with relative elevation, H_R, defined as $H_L - H_{avg}$, where H_L is the local elevation, and H_{avg} is the average elevation of a square region surrounding the local point (a search box

Table 1. Flow Chart of Our Analysis Steps

Analysis Step	Input Data	Procedures	Results of Analysis
1. Define drainage network	128 pixel/degree MOLA DEM with post-Noachian craters removed	a. Reduce DEM resolution to 32 pixels/degree b. Route flow through network for a range of assumed *X*-values	A 32 pixel/degree map of the active drainage network for each *X*-value
2. Map valley networks	256 pixel/degree MOLA DEM overlaid on 256 pixel/degree THEMIS IR mosaic	Digitize valley networks	Individual valley segments represented as longitude-latitude pairs
3. Determine depth of valley incision	a. Digitized valley network b. MOLA shot data	a. Use automated procedure to identify suitable valley segments based on regularity of valley topographic profile	Database of valley segment locations, depths of incision and valley gradients
4. Route flood discharges	a. Active drainage network from Step 1 b. Assumed degree of orographic effect on runoff and degree of flood attenuation in lakes c. 32 pixel/degree MOLA topography	a. Use criteria to determine real versus DEM artifact lakes b. Route relative flood discharges for a range of assumed *X*-values	32 pixel/degree database of relative flood discharges for a range of *X*-values
5. Correlate depth of valley incision with calculated discharge and valley gradient	a. Relative flood discharges from Step 4 b. Incision database from Step 3	Bivariate and multiple correlations analysis between incision depth, relative flood discharges, and valley gradient	Exponents, regression constants, correlation coefficients and R^2 values for a range of *X*-values
6. Measure cumulative valley volume and average basin gradient	a. Flood discharges from Step 4. b. 128 pixel/degree MOLA DEM with post-Noachian craters removed	a. Route cumulative valley volume downstream by accumulating measured local valley volumes, with volumes being reset if a real lake is encountered b. Determine value of average valley gradient upstream from each location.	32 pixel/degree database of local and cumulative valley volume and local and basin-averaged valley gradients for a range of *X*-values
7. Correlate local and cumulative volume of valley incision with valley and basin gradients and flood discharges	a. Database of local and cumulative valley volumes and gradient from Step 6 b. Relative flood discharges from Step 4	Bivariate and multiple correlations analysis between erosion volume, relative flood discharges, and valley gradient	Exponents, regression constants, correlation coefficients and R^2 values for a range of *X*-values
8. Examine spatial variation in estimated valley volume and relationship to regional topography and latitude	a. Database of local and cumulative valley volumes and gradient from Step 6 b. Relative flood discharges from Step 4	a. Divide database and discharge databases into regional cells about 1066 km by 1066 km. b. Calculate average elevation, regional gradient, and relative roughness for each cell c. Analyze spatial variation of valley volumes, estimated discharge, and cell topographic properties by correlation and spatial mapping	Spatial variations in valley incision and related topographic and flood discharges.

of 100×100 km). Temperature, runoff, and evaporation data also show similar correlation with relative elevation, thus H_R was used in the regression instead of the actual elevation. Other effects, such as rain shadowing, are not accounted for in this relationship. The relationship for the *X-ratio* was derived first by using linear regressions for H_R versus runoff, precipitation, and evaporation data collected for the Great Basin region (Figure 2, "Great Basin Regression"). This relationship was then approximated by the formula

$$X + 1 = e^{a+bH_R}, \tag{5}$$

where $a = 2.027$ and $b = -0.00216$ for the Great Basin (Figure 2, "Exponential Fit"). This relationship was utilized for a series of simulations of runoff and lake levels (pl) on Mars for different *X-ratios*, where the multiplicative constant b was held constant, but the value of a was chosen to match the assumed *X-ratio* (6.2 for Figure 2) for a flat surface ($H_R = 0.0$). Figure 3 shows values of H_R for a portion of the southern Isidis basin rim and its effect on runoff pattern. Simulations of runoff and lake levels were also conducted for a smaller dependency of *X-ratio* on H_R with $b = -0.00107$. Elevation dependence for Mars might be different from the Great Basin. It is not our intent to assert that there was an orographic effect, much less formulate the exact relationship; hence, we used three different dependency values, b, (including no elevation dependency, $b = 0$) to examine the effect of different degrees of orographic control on precipitation. The results from atmospheric models suggest that the topography is one of the main factors controlling the distribution of surface temperature and precipitation on Mars under a denser atmosphere [*Forget et al*., 2013; *Wordsworth et al*., 2013]. Thus, we are testing whether an assumption of orographic effects gives better explanation to the relationship between the climatic conditions and the spatial pattern of valley incision. Our approach is a simple, but diagnostic method of

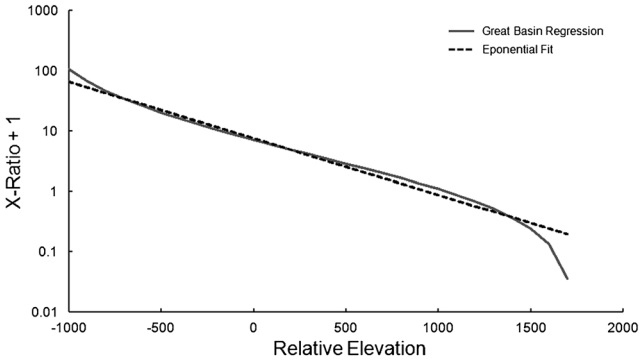

Figure 2. Relationship between relative elevation, H_R, and *X-ratio* for the Great Basin region of the southwestern U.S. defined by regression of precipitation, runoff, and evaporation versus H_R ("Great Basin Regression"). This regression was approximated by an exponential relationship ("Exponential Fit", equation (5) in text).

examining the effects of orographic control on precipitation; direct coupling of predictive models of orographic effects with climate models offers a promising approach for future work [*Scanlon et al.*, 2012].

[21] We assume that for simulations using the elevation-dependency in equation (2), that the equation defines both mean annual flows defining the drainage network and the runoff depth for flood events.

4.1.2. Flood Attenuation

[22] Our default flood routing through the drainage network assumes that flow magnitude is not affected by passage through a lake. It is observed, however, that terrestrial floods become diminished in passing through a lake or reservoir in proportion to the size of the water body [e.g., *Basha*, 1994; *Horn*, 1987; *Kessler and Diskin*, 1991; *McEnroe*, 1992; *Miotto et al.*, 2007]. We explore the effects of flood attenuation in some simulations such that if a high runoff event enters a lake that is overflowing, the runoff exits through the lake outlet, but the temporary storage attenuates the downstream flood peak.

[23] Observations of flood attenuation in terrestrial lakes and reservoirs [*Basha*, 1994; *Horn*, 1987; *Kessler and Diskin*, 1991; *McEnroe*, 1992; *Miotto et al.*, 2007] suggest that the magnitude of the attenuation is related to the ratio of the incoming discharge to the lake area. Lakes considered false suffer no attenuation of discharge or interruption of downstream sediment routing. For lakes considered "real", the model for flow attenuation is

$$Q_{OF} = Q_{IF} e^{[-K_A(A_{LA}/Q_{IA} - 1/R_C)]}; \quad A_{LA}/Q_{IA} > 1/R_C\,, \tag{6}$$

where Q_{OF} is the flood peak magnitude downstream from the overflowing lake, Q_{IF} is the sum of input flood discharges to the lake, and K_A determines the rate of increase in attenuation as A_{LA}/Q_{IA} exceeds $1/R_C$. We utilize three levels of flow attenuation, $K_A = 0.0$ for our default routing with "no attenuation", $K_A = 10.0$ for "medium attenuation", and $K_A = 1000.0$ for "high attenuation." Again these values are arbitrarily assigned to explore the wide range in degree of downstream diminishment of discharge that allows us to determine the degree to which attenuation affects the relationship between the climatic conditions and incision depth.

[24] Lakes are efficient sediment traps. For eroded sediment being routed through the fluvial system (discussed below) we utilize the distinction between real and false lakes

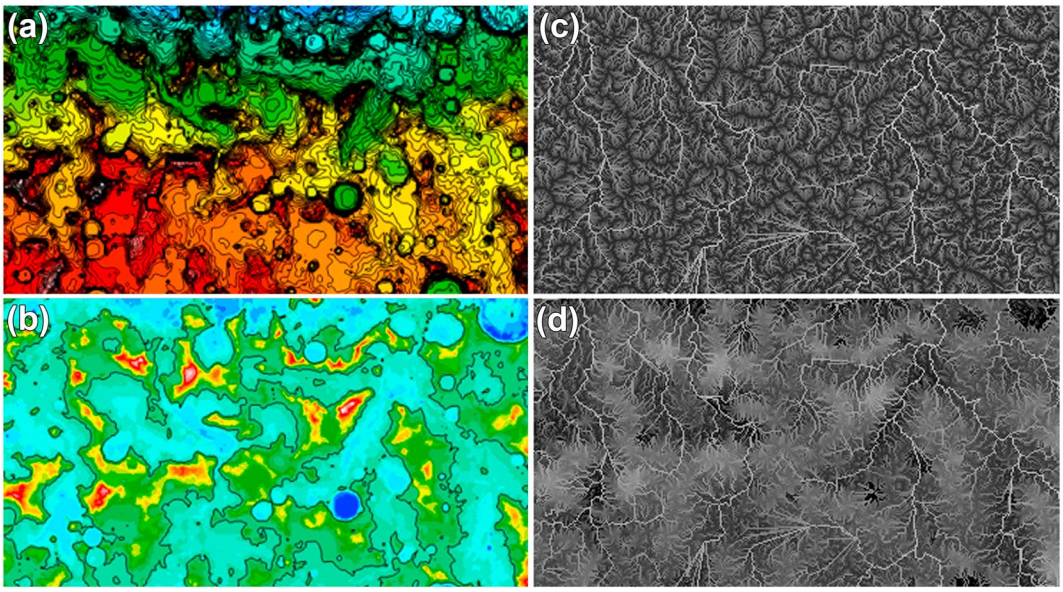

Figure 3. Effect of elevation-dependency of runoff on valley network discharges for a portion of the southern Isidis Basin rim. (a) Elevation map. Elevation range from −4000 to 3000 m. Image width about 719 km. (b) Relative elevations, H_R, defined by deviations from the average of a 100×100 km box. Zero value of H_R is contoured, and the range of values is from −2000 to 3000 m. Elevation-dependent runoff increases with H_R by equation (5). (c) Discharge map based on uniform precipitation (lighter colors imply greater flows). (d) Discharge map based on elevation dependent precipitation. Note that runoff contributions are dominated by high relative elevation regions.

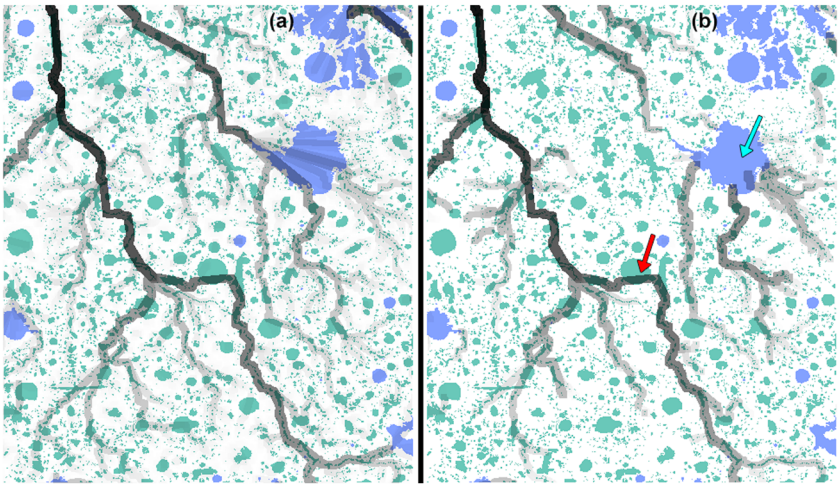

Figure 4. Map of the Samara, Parana, and Loire Valles region showing modeled flood discharge and cumulative valley volume. (a) Relative flood discharges shown in shades of grey. Width of valleys exaggerated for clarity. Darker colors indicate greater flow magnitude. Flooded depressions considered to be actual lakes are shown in blue, whereas depressions in green are considered to be artifacts of DEM creation and post-Noachian modification of the valley network. Flood discharges pass through both actual and false depressions, although in some simulations flow magnitude is attenuated in lakes. (b) Cumulative valley volume routed through the drainage network, with greater volume in darker grey. Lakes considered to be actual lakes (e.g., the Parana Basin at the cyan arrow) are assumed to be sites of deposition of sediment eroded from valleys, so that valley volume is reset to zero. At lakes assumed to be artifactual (red arrow) eroded sediment is assumed to be routed downstream and the cumulative volume is not reset. The drainage network and lakes are shown for an *X-ratio* of 3.1. Same region as shown in Figures 1 and 10.

described below. Similarly, false depressions had no effect on sediment throughflow, but all sediment entering real lakes was deposited, that is, a "total attenuation."

[25] The reduction of discharge by flood attenuation is assumed to affect only the routed floods and not the extent of the drainage network as defined by the mean annual flow.

4.2. Defining Valleys

[26] To quantify incision, valley networks were identified and delineated using two separate methods: (1) a hydrologic routing model and (2) mapping of valley networks (Figure 1). The hydrologic routing model uses MOLA DEMs from which post-Noachian craters have been replaced by a smooth surface [*Matsubara et al*., 2011] to determine flow direction. To route water with available computer resources, the DEM was reduced in resolution from its original 128 pixels/degree to 32 pixels/degree (~1.85 km/pixel at the equator) by selecting the lowest elevation within the equivalent higher-resolution cells to preserve the best hydrologic connectivity possible. The drainage network was automatically delineated by steepest-descent pathways, with overflow at the lowest point of enclosed depressions. This drainage mapping approach is similar to that used by *Luo and Stepinski* [2009].

[27] Valley networks were also mapped using a layered Geographical Information System (GIS) database of Mars Odyssey Thermal Emission Imaging System (THEMIS) daytime IR images, the Viking Orbiter Mars Digital Image Mosaic 2.0, and the Mars Global Surveyor Mars Orbiter Camera wide-angle image mosaics (all overlaid at a 232 m/pixel resolution), with a contour map based upon MOLA Precision Experiment Data Record (PEDR) data with a 1 km^2 grid. This mapping approach was similar to, but independent of, the valley network map by *Hynek et al*. [2010]. In many cases valleys could be followed by aligned contour bends in the DEM even where post-Noachian degradation had obscured the visibility of the valley. On the other hand, where valleys were visible, the image database generally provided a more accurate location of the valley centerline than the contour map.

[28] In general, the DEM-based routing and manual mapping produced nearly identical pathways (Figure 1), although the DEM-based routing generated a more extensive network extending closer to drainage divides. In a few locations the two methods yielded significantly diverging flowpaths, often due to post-Noachian surface modification (e.g., impacts, mass wasting) or from resolution limits and/or gaps in the MOLA DEM that produced artificial depressions (most commonly occurring in low-gradient, low-relief portions of the valley network). Examples of such occurrences in terrestrial flow routing are discussed in *Matsubara and Howard* [2009].

4.3. Defining Real Versus False Lakes

[29] A limitation of the MOLA DEM when used for the flow routing is that it introduces artificial depressions. Several factors contribute to such "false" depressions: (1) local wide spacing between the MOLA tracks utilized to create the DEM; (2) reduction in grid resolution necessary to route flow and sediment through the drainage networks; and (3) post-Noachian valley modification, particularly by impact cratering. We attempt to partially account for post-Noachian craters using a "healing" procedure by replacing such craters and their ejecta in the DEM used for flow routing with a smooth surface as discussed in *Matsubara et al*. [2011]. It is important to distinguish between "real" and "false" depressions, the latter of which should have no attenuation effect upon

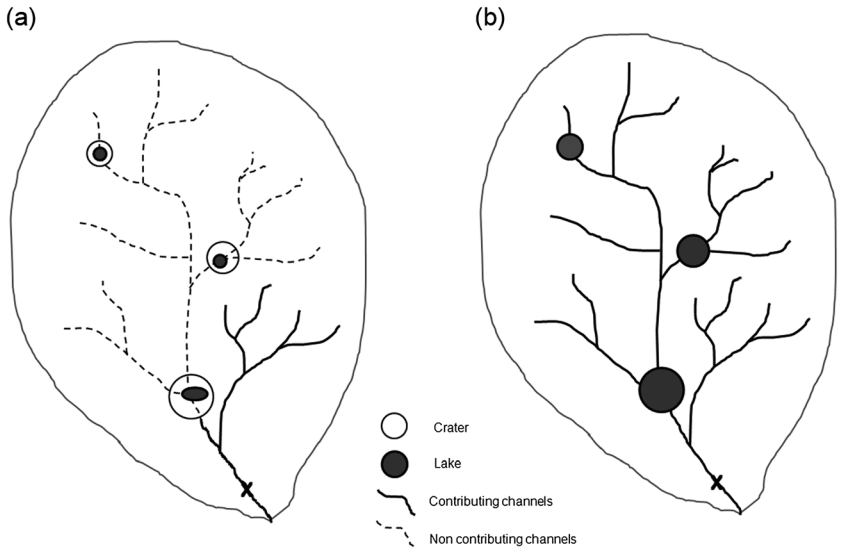

Figure 5. Schematic diagram showing the changes in number of channels contributing to the discharge at a point of interest, *X*, under (a) dry (high *X-ratio*) and (b) humid (low *X-ratio*) conditions.

flow or sediment throughflow. The distinction between real and false lakes is particularly important for sediment routing through the network, because lakes are assumed to capture all incoming sediment. To identify and remove "false" depressions in the flow routing model we defined multiple criteria that simulated lakes must meet to be "real." First, we set an upper limit of lake area for possible false lakes at 2500 km^2 based on the annual flow routing. Then for simulated lakes smaller than this threshold, we use two criteria for defining false lakes, such that satisfying either criteria results in the lake being considered "false." The first criterion utilizes the ratio $R_{QA} = Q_{AI}/A_{LA}$ as a discriminating index, where A_{LA} is the area of the lake and Q_{AI} is the annual discharge into the apparent lake from upstream (using the 1 m assumed runoff depth). Using $R_{QA} > 50$ identifies most depressions located along major valley networks as false depressions. The second criterion is the ratio $R_{VA} = V_{LA}/A_{LA}^{1.5}$, where V_{LA} is the lake volume. Lakes are considered to be false for $R_{VA} < 0.02$. The actual values of these criteria were selected after trial and error to assure flow connectivity along major valley networks for moderate *X-ratios*. In addition, a few disparities between the mapped valley network path and the flow routing path resulted in the routed flow to enter a real lake. An example occurs at location 3 in Figure 1. In five such situations the depressions were specified to be false (including the depression at the red arrow in Figure 4).

[30] In the flow and eroded volume routing through the fluvial network, false depressions have no effect on flow or transport, but real lakes can result in flow attenuation as discussed above and real lakes are assumed to trap all routed eroded volume.

4.4. Using Relative Discharge

[31] In most terrestrial drainage networks, lakes are rare and the discharge, *Q*, can usually be approximated by a simple power function of upstream contributing drainage area [*Howard*, 1994]. On Mars, however, drainage integration was poor because of interspersed depressions, mostly due to impact craters. Thus, parts of the potential upstream drainage area might not actually contribute to streamflow because evaporation in lakes occupying basins reduces the amount of overflow into downstream basins (Figure 5a). As a result, the discharge is less than what would result when all potential upstream area contributes to the flow (Figure 5b). The effect of lake connectivity on discharge downstream is shown in Figure 6, which is a plot of the relative discharge averaged for a number of valleys in the Isidis region of Mars expressed as a ratio of the simulated discharge for each value of the *X-ratio* that would occur if all potential upstream areas fully contributed to the flow (that is, if all depressions were filled to overflow conditions). For an *X-ratio* of −1 (wettest condition with no evaporation), all areas contribute so that the relative discharge is 1. As the *X-ratio* increases and the climate gets drier, the upstream region would stop contributing to the downstream region because of the lakes intercepting the flow

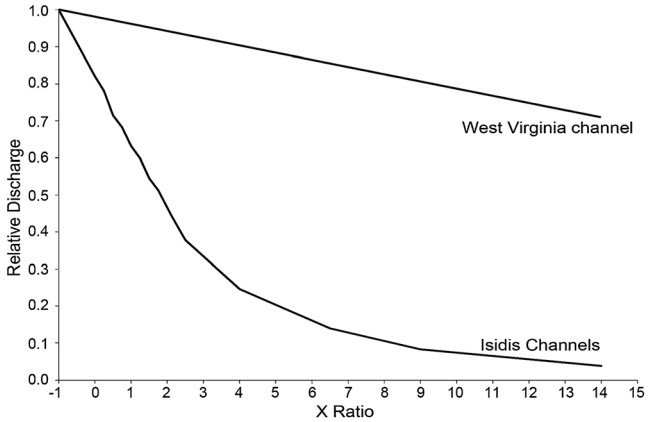

Figure 6. Changes in average relative discharge ($Q_{(x)}/Q_{(x=-1)}$) for the Isidis region (blue) and an average terrestrial channel in West Virginia channel (red) with respect to the assumed *X-ratio*.

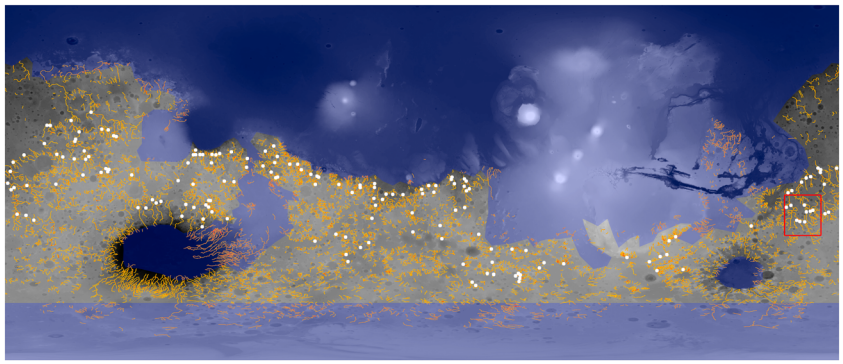

Figure 7. Orange lines show valley networks mapped using GIS database of image mosaics and MOLA-derived contours. Elevations shown in shades of grey. Areas excluded from analysis because of high latitudes, young geologic age, or location in major basins (Hellas and Argyre floors) are shaded in blue. White dots show valley network locations sampled for analysis of estimated discharge as a function of the *X-ratio*. Simple latitude-longitude projection excluding regions north of 64°N. Red box at right shows location of Figures 1, 4, and 10.

and the relative discharge decreases rapidly. In contrast, for integrated terrestrial drainage networks lacking appreciable lakes, the relative discharge drops more gradually over the range of the *X-ratios* (Figure 6).

[32] The number, magnitude, and duration of flood discharges excavating the Martian valley network is highly uncertain. Post-Noachian modification of valleys by partial aeolian infilling, mass-wasting, and impact cratering has largely erased information on channel morphology that could be used to scale discharge magnitudes. A number of local channel segments are exposed, permitting estimates to be made of channel width. Together with assumptions about channel depth and roughness, these have permitted order-of-magnitude estimates of channel-forming discharges [*Irwin et al*., 2005a; *Jaumann et al*., 2008; *Moore et al*., 2003]. However, such channel exposures are rare, so that absolute magnitudes of flood discharges cannot be well constrained. Climatological modeling of early Mars is also unable at present to constrain precipitation magnitudes. The approach adopted here is to examine the pattern of valley incision using simulated relative flood discharges. We assume that runoff from precipitation events is areally uniform (or alternatively has an orographic elevation dependence, as discussed above). We assume an arbitrary runoff depth and route the flow through the drainage network, and compare the spatial pattern of simulated runoff to the depth and volume of valley incision using multivariate regressions of the form of equation (4). Although the absolute magnitude of flood events is uncertain, the spatial variation in flows is constrained by valley network geometry, and the spatial pattern of valley erosion can be correlated with the spatial variation of simulated relative flood discharges. Thus, although the absolute magnitude of the regression coefficient, K, in equation (4) is uncertain, we assume that it is spatially invariant so that the exponents in the regression can be estimated and the degree of fit of the equation as measured by the percentage variation of the independent variable be explained by the regression (R^2). By looking at

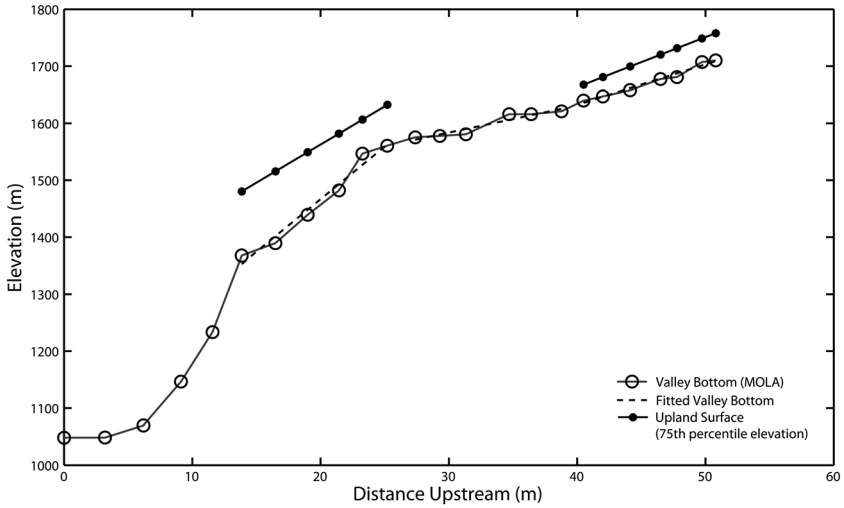

Figure 8. An example of a valley profile (solid line with open circles). The dashed lines are the best-fit lines to segments of the valley profile and solid lines with closed circles are the best-fit trends of the surround uplands. Valley incision is estimated from the difference between the two fitted lines. The middle dashed line does not have an upland fitted line because it did not meet the channel selection criteria.

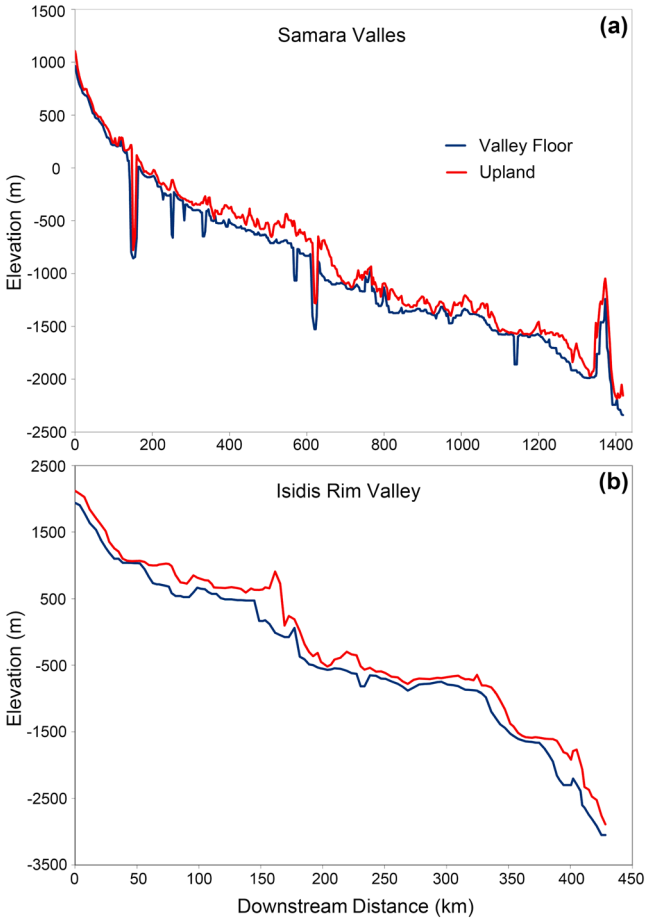

Figure 9. Representative Martian valley profiles. "Valley Floor" is the lowest elevation of the valley interior within a search radius of 4 km. "Upland" is the 75th percentile elevation within a 4 km search radius. (a) Samara Valles has a generally smooth, concave profile suggestive of a fully alluvial channel. Low points along profile are superimposed impact craters, and the local highpoints are generally filling by postflow crater ejecta. Highpoint near end of valley is a volcanic construct [*Grant and Fortezzo*, 2005]. (b) Valley on the southern interior rim of the Isidis Basin. The steep reaches of the stepped profile occur primarily where the valley cuts through rim massifs, and are probably either bedrock or boulder-bed alluvial channels. Gentler reaches are probably fine-bed alluvial channels graded to the bedrock/boulder reaches.

the relative discharges and how they change with *X-ratio*, we can find if the amount of valley incision can be explained by the spatial patterns (e.g., upstream discharge vs. downstream discharge) of relative discharge and valley gradients, which in turn may be informative of climatic conditions at the time of valley incision.

[33] For convenience, we assume that the flood runoff depth is 1 m, so that the estimated flood discharge (in m^3 per unit time) is proportional to the effective upstream contributing area. For an *X-ratio* of −1, the simulated discharge is numerically equal to the entire upland area that would contribute flow if all depressions were overflowing and no en route evaporation or infiltration occurs. For higher *X-ratios* the simulated discharges can be considered to be numerically equal to an effective contributing area partially isolated by nonoverflowing upstream lakes.

4.5. Quantifying Valley Incision Depth

[34] Estimates of valley incision were derived from algorithms that identified valley segments with readily quantifiable incision depths. This automated process produces a global database of 12,043 selected reaches throughout the Noachian highlands (Figure 7).

[35] The algorithm uses the digitized valley network data discussed above to examine individual valley sections (generally valley links between tributary junctions) by fitting a least-squares regression line through a specified valley segment (Figure 8). Within each valley segment, the selection procedure progressed upstream from each selected reach until the upstream end of the segment was reached. Similar fitting to the surrounding uplands determined if the reach had a definable upland surface into which incision occurred. The fitted lines were then examined using several selection criteria, which had to be simultaneously satisfied: (1) a minimum path length of the selected valley segment, (2) a minimum number of digitized points in the segment, (3) a minimum correlation between the digitized valley profile points and the fitted line, and (4) a maximum standard error of estimate for the regression line. We generally required valley segments to (1) be at least 10 km long, (2) slope downstream, (3) contain at least 5 digitized points defining the valley, (4) have a correlation coefficient greater or equal to 0.8, (5) have a standard error of estimate not exceeding 50 m, and (6) be Noachian in age and incised into nonvolcanic materials (based on geologic map). As a result, only reaches with smooth valley bottom and upland surface profiles are included in our database to minimize the effect from post-Noachian impacts and mass wasting.

[36] The final criterion that a selected valley segment had to meet involved the simulated drainage network. The estimated discharge is based upon the flow routing algorithm of *Matsubara and Howard* [2009] and *Matsubara et al.* [2011], and although these simulated flow routes, as discussed above, are generally in accord with the digitized valleys, there are some local differences due to factors such as gaps in MOLA data and post-Noachian impact craters. Thus, selected reaches were eliminated if they could not be matched with the valley path predicted by the flow routing model within a 2 pixel radius (3.7 km), or if the reach is predicted to have been submerged under the *X-ratio* = 4 conditions that we utilized as a baseline.

[37] Local estimates of the depth of valley incision were made by measuring the difference between the elevation of the valley bottom and the elevation of the surrounding uplands as discussed by *Howard* [1994] and *Howard et al.* [2005] (Figure 8). The upland surface for each location was defined as a specified percentile elevation for all MOLA shots (using the global database of MOLA PEDR shot data) falling within a square box centered on each digitized valley bottom location [*Howard et al.*, 2005]. Using the MOLA PEDR data allows us to avoid artifacts from DEM generation and also permits us to eliminate valley reaches with an insufficient number of PEDR shots to evaluate the valley bottom and cumulative elevation distribution for any search box. We evaluated search boxes of 8, 16, and 32 km edge size around the selected points and various percentile

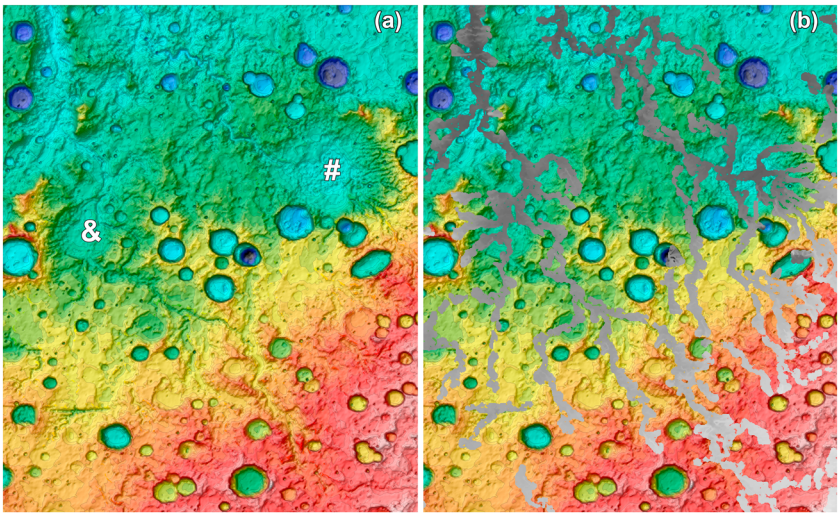

Figure 10. Map of the Samara, Parana, and Loire Valles region. (See Figure 7 for location). (a) Elevation-coded shaded relief image. (b) Grey overprint shows valleys defined by the 75th relative elevation in a 16 × 16 km sample box centered on the valley bottom. Disconnected sample locations were joined by downstream routing in erosion volume calculations. Valleys are generally sharply incised below an upland surface defined by the nongreyed areas in Figure 10b. Region is the same as that shown in Figures 1 and 4. Map width about 765 km, centered at 343.7°E 24.9°S. Locations "#" and "&" are discussed in text.

elevations. If a box that is too small was utilized, then the search would not extend beyond the valley walls, and incision depths and incision volumes would be grossly underestimated. On the other hand, if the box was too large, then the depth and volumes of incision could be overestimated by including topography not immediately adjacent to the valley rim. For this study, we used the 75th percentile elevation within a 16 km box as a representative upland elevation. The use of the 75th percentile elevation rather than the maximum or the 90th percentile elevation within the search radius avoided biasing due to local high points such as crater rims.

[38] This automated process of reach selection enables us to create a much larger, more spatially extensive database than could be generated by manual inspection in a reasonable amount of time. However, the automated process could result in inclusion of strongly modified valley segments or locations lacking a well-defined initial surface into which the networks were incised. A few regions on Mars were analyzed using manual selection of valley segments, and they provided results similar to the automated process. The results from the manual analysis (results not shown), albeit limited, indicate that the automated selection process produced an unbiased sampling of valley reaches.

[39] Our selection procedures eliminate almost all cases where kilometer-scale or larger post-Noachian cratering has modified valley profiles because of the specification that for selected reaches both the valley and upland have to be nearly parallel profiles and be of near-constant gradient. Valleys have also been affected by mass wasting, aeolian infilling, and impact gardening by small bolides. These diffusive processes result in underestimation of the depth of incision, but the regular profiles of both valleys and uplands where unaffected by large craters (e.g., Figure 9) suggests these modifications are spatially nearly uniform, and thus introduce a small, but systematic underestimation of the amount of valley incision.

5. Results

5.1. Plausible X-ratios

[40] We selected 170 relatively large valley networks that are incised considerably below the Martian highland surface to estimate the range of *X-ratio* most likely responsible for the formation of the valley networks. The selected reaches are located close to the apparent downstream end of each valley network so that the simulated discharges would be sensitive to the overall basin topography, particularly upstream depressions that would either overflow or not depending on the assumed *X-ratio* (white dots on Figure 7). For larger drainage networks, like the Samara-Loire system (Figure 10), major tributaries near their downstream terminations were also sampled. For each of the selected valley sites we plotted simulated discharge against the *X-ratio* (e.g., Figure 11). This analysis assumes spatially uniform values of the *X-ratio* within each basin containing a valley network, except for some simulations where spatial variation was induced by an assumed orographic effect. We also assumed no flow attenuation within upstream lakes.

[41] Each valley network is characterized by a relationship between the simulated discharge and the assumed *X-ratio* (e.g., the Isidis channels in Figure 6) such that the discharge increases as the *X-ratio* gets smaller as additional runoff from upstream portions of the drainage network contributes through lake overflow (Figure 5). We examined each plot and noted the largest (driest) *X-ratios* that characterize each of the following criteria: (1) where the discharge exceeded 50% of the maximum discharge (Q_{max}) for the valley; (2) where discharges reached 5% of the maximum; and, if there is any, (3) where a lake covering the sampling location first formed (Figure 11). These percentage thresholds can also be interpreted as a fractional amount of the maximum possible upstream contributing area that is contributing flow for the corresponding *X-ratio*. For most valleys discharges remained

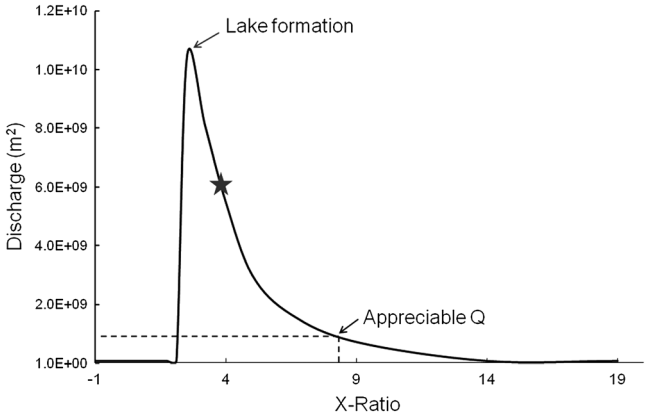

Figure 11. Example of the modeled discharge through a valley site as a function of the *X-ratio*. The analysis determines the *X-ratios* at specific ratio values of modeled discharge relative to the largest modeled discharge. In most cases the largest discharges occurs at an *X-ratio* of −1.0, but in the case illustrated a lake is formed at an *X-ratio* of ~2.0. The 5% of Q_{max} value is shown, and the star indicates the 50% of Q_{max} value.

very low as the assumed *X-ratio* decreased until a threshold value (e.g., 5%) was reached. As the *X-ratio* becomes smaller, the discharge increases rapidly (Figure 11). Because valley incision required appreciable water flows, defining these critical values of *X-ratio* provides a simple assessment of climatic conditions needed to form the valley networks.

[42] The results for all of the 170 networks are summarized as a cumulative plot that shows the fraction of drainage basins reaching each of the above thresholds as the assumed *X-ratio* was decreased (Figure 12). As expected, the number of valleys attaining a high fraction of the maximum contributing area increased rapidly as *X-ratio* was reduced. With an *X-ratio* of 1, most of the valleys received appreciable flows. We do not know what the formative discharge was for any of the valleys on Mars; however, it is most likely that considerable size of flood was necessary to form valley networks. When series of plots like Figure 11 were studied, discharge started to increase more rapidly after reaching about 5% of Q_{max} indicating some of the small lakes are starting to overflow. The plot of the cumulative number of times that each event occurred as a function of decreasing *X-ratio* shows that, even to have half of the selected valley networks to have discharge of about 5% of Q_{max}, *X-ratio* needs to be as low as 4.5 (Figure 12 black solid line). It took *X-ratios* of 3 and 2 to have, respectively, 80% and 90% of the selected channel to sustain discharge of 5% of Q_{max}. The actual formative discharges probably were much larger, hence using of low discharge (e.g., 5% of Q_{max}) could improve our analysis to constrain the *X-ratio* required to yield discharge responsible for valley incision. Also, lakes in impact craters and other depressions started to overflow around *X-ratio* of 4, which led to integration of valley networks upstream and downstream of the lake. The simulations with orographically dependent runoff (labeled "5% of Q_{max} (with strong topographic effect)" in Figure 12) resulted in appreciable flows at higher *X-ratios* than for simulations with no elevation dependency.

[43] Figure 13 shows the spatial distribution of the *X-ratios* necessary for individual valleys to reach 50% of their maximum flow. There is not a strong pattern in the results except that generally low *X-ratios* are required to attain large discharge in the region from 30°S to 20°N and 0–45°E. This is a fairly low gradient region with a sparse drainage network where valley network is less integrated, including the Evros Valles system (12.56°S, 13.67°E).

[44] In summary, our appreciable discharge analysis shows that to form the valley networks we see today, the highlands of Mars probably experienced climatic conditions equivalent to an *X-ratio* of 4 or lower. This condition is similar to those experienced by northern Great Basin during the last glacial maximum. If the orographic effect similar to the one experienced by the Great Basin region occurred on Mars, this range could be shifted upward. This result is in accord with the range of *X-ratios* that we had estimated in our previous study based on the overflow of lakes [*Matsubara et al.*, 2011], further constraining the plausible *X-ratio* range.

5.2. Valley Incision Estimates

[45] The rate of bedrock channel incision is commonly modeled as a function of flow intensity, such as shear stress or stream power [*Howard and Kerby*, 1983; *Howard*, 1994; *Whipple and Tucker*, 1999, 2002]. Through the use of formulas for flow resistance and channel dimensions, the incision rate can be expressed in the form of equation (4) using estimated incision depth, I, as the dependent variable and local valley gradient S_V and relative discharges Q_F estimated from hydrologic simulations for 18 specific assumed values of the *X-ratio* as the independent variables

$$I = KQ_F{}^m S_V{}^n, \tag{7}$$

where K is a constant dependent on flow frequency and intrinsic bedrock erodibility, and m and n are exponents that

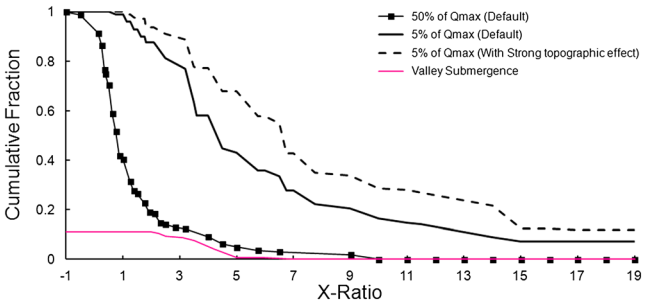

Figure 12. Cumulative frequency histogram of *X-ratios* at which 170 downstream valley network locations experienced the specific value of discharge relative to the maximum discharge occurring for low *X-ratios*. About 12% of the valley locations became submerged at low *X-ratios*. The curve labeled "5% of Q_{max} (with strong topographic effect)" was for flow modeled with elevation-dependent *X-ratios*, with a value of $b = 0.00216$ in equation (5). The other curves represent simulated discharges with spatially uniform *X-ratios*. For a specific flow frequency the valley networks with elevation-dependent runoff (higher runoff from elevated portions of the drainage basin) reached a given flow fraction for higher *X-ratios*.

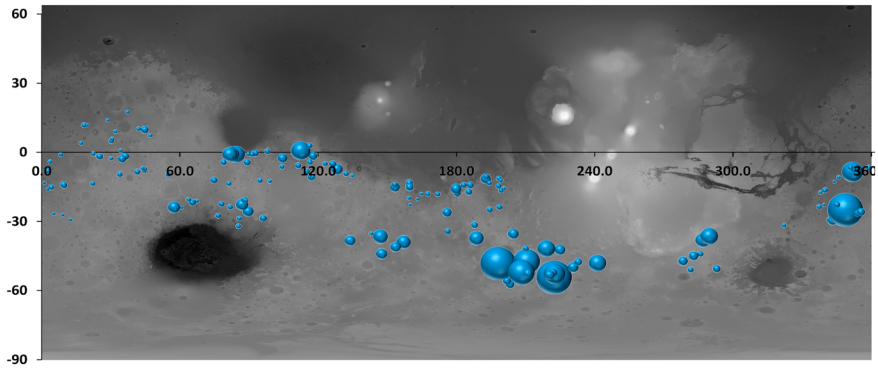

Figure 13. Spatial distribution of the relative *X-ratios* for which the 170 sampled valley network locations reached 50% of their maximum flow at low *X-ratios*. Bubble size is proportional to the *X-ratio* ($0.5 \leq X\text{-}ratio \leq 10$).

can be theoretically derived or empirically estimated. In this study, the values of *m* and *n* were derived empirically using the gradient and estimated discharge data. The assumptions, limitations, and terrestrial applications of modeling stream incision as a power function of stream power are discussed in *Howard* [2007], *Barnhart et al*. [2009], and *Howard and Tierney* [2011]. If a region experiences an areally uniform climate, then the depth of incision throughout the network can be correlated with estimated discharges and valley gradients to statistically define the constant and exponents in the above relationship in terms of a long-term average incision rate.

[46] The regression utilized observations made throughout the Martian highlands for valley reaches representing a wide range of incision depths, valley gradients, and upstream versus downstream locations within the valley networks. Because our hydrological model is not a dynamical model where floods and the resulting erosion events are modeled sequentially, we are only looking at the relative spatial variability of flood discharges and the long-term resultant incision depths. To apply equation (7) to valley incision, we make the following assumptions: (1) within a given region all the valleys experienced the same long-term climatic history, so that the measured incision reflects the summation of individual effective flows through the drainage network; (2) the values of discharge that we estimate are, of course, not the actual discharges, but they are assumed to reflect the spatial variation of effective discharges (that is, the downstream hydraulic geometry of flow variation [*Leopold and Maddock*, 1953]); (3) the estimated incision depths correspond to a planet-wide period of incision into a well-defined initial surface (observations suggestive of such a history are presented in *Barnhart et al*. [2009], *Howard et al*. [2005], and *Carr* [2012]). Because only the relative magnitude of discharges within the drainage networks is predicted by the flow routing model, the value of the multiplicative constant, *K*, in equation (7) for regressions involving discharge is relative rather than absolute. However, the value of the exponents, β_i (*m* and *n* in equation (7)) and measures of goodness of fit (single or multiple correlation coefficients and *t* statistics of significance for estimated exponents) reflect the degree of association between spatial variations of the response variable (e.g., depth of incision) and associated predictor variables (e.g., valley gradient and estimated discharge). Possible limitations to the validity of these assumptions are discussed in section 6.3.

[47] The relative success of equation (7) in estimating incision depths can be expressed as the regression R^2 value. The relative role of estimated discharge, Q_F, and of the valley gradient, S_V, in the regression can be measured by the "*t*" statistic (5% level of significance) for the estimated exponents, *m* and *n*, with higher values indicating greater significance (Figure 14). We use the R^2 values and *t*-values to find which value of the *X-ratio* best explains spatial patterns of incision depths.

[48] The regression analysis was conducted on the 12,043 reaches selected by the automated process described earlier initially using the discharge estimated without orographic or flood attenuation effect. The results showed that the R^2 value, which is for the whole regression, remained almost constant for all values of *X-ratio*, whereas the value of *t* for the *m* exponent decreased with increasing *X-ratio* value (Figure 14). Both the R^2 values and the *t*-values suggest that the best fit for incision depths occurs for *X-ratio* less than 4 (Figure 14). This optimum *X-ratio* range also coincides well with the predicted values from our previous basin overflow analysis [*Matsubara et al*., 2011]. The estimated

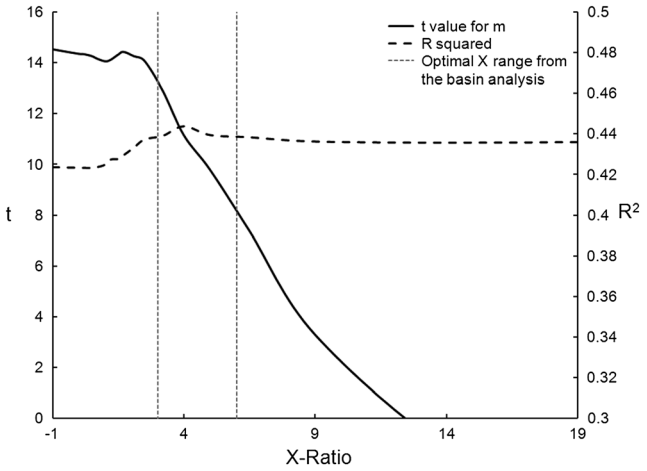

Figure 14. Degree of explanation of spatial variation in valley incision as a function of the *X-ratio* as measured by the regression R^2 value (right axis) and the "*t*" measure of significance of the estimated exponent, *m* (left axis). Both values indicate that the best fit for incision depth occurs for relatively low *X-ratios*.

Table 2. Regressions of Estimated Incision Depth Upon Local Gradient and Modeled Relative Discharge, With R^2 Being the Fractional Explained Variance of the Multiple Regression. K, m, and n Are Coefficients in Equation (7)

Analysis Method		R^2	K	n	m	# of Reaches
Global		0.43	6.06	0.57	0.03	11305
Regional (12 regions)		0.25	5.86	0.38	0.01	848
Discriminant function		0.39	5.77	0.49	0.04	1328
Flood attenuation	(low - med)	0.43	6.53	0.56	0.03	11305
	(high)	0.44	6.54	0.57	0.03	11305
Orographic effect	(Moderate)	0.42	5.83	0.5	0.03	1989
	(Strong)	0.41	5.88	0.49	0.03	1896

values of exponents, m and n, are on average around 0.03 and 0.57, respectively (Table 2). Figure 15a shows the relationship between incision depth and valley gradient for an *X-ratio* of 2.7. A similar plot between incision depth and estimated discharge yields just a cloud of points because of the low correlation. These results imply that, although both estimated exponents are statistically different from zero, the contribution of spatial variation in estimated discharge to the regression is minor relative to variations in the valley gradient. Similar results were obtained using discharges reduced by attenuation and adjusted for orographic effects (Table 2). The effects of either flow attenuation in lakes or orographically influenced precipitation pattern have negligible influence on the spatial pattern of incision.

[49] A similar analysis was conducted at the regional scale. Mars was divided into regional cells as it was for the previous lake overflow study (1000 km × 1000 km cell size at the equator with 50% overlap with adjacent cells). One cell in Aeolis region, which contains the downstream end of Al-Qahira Vallis, resulted in higher exponent value for discharge ($m \sim 0.15$) for *X-ratio* of 2.5 or lower. However, all of the other cells resulted in the same m and n values as the global analysis indicating that discharge is not a major contributor to the regression. The same conclusion was reached for 12 regions (865 reaches total) where reach selection was conducted manually.

5.3. Volume of Erosion

[50] The eroded volume of a valley system is an index of the cumulative magnitude of fluvial erosion. The volume of valley per unit valley length is a measure of valley cross-sectional area, A_V, and when this area is summed downstream it becomes a measure of total upstream erosion, V_T, and the volume of sediment that had to have been transported through any given location along the valley network. In this section we relate A_V and V_T to basin gradient, estimated discharge, and topographic characteristics on both a global and regional basis.

[51] We utilize the DEM-based routing methodology discussed earlier to route estimated eroded volumes downstream. Unlike the restrictive criteria for valley segment selection used in the incision depth analysis, all DEM-defined valleys and drainage basins were potentially included in the present analysis. However, to minimize inclusion of undissected uplands and various types of linear depressions and structural features that lack recognizable features of eroded valleys, we limited our selection to those basins containing mapped valley networks (Figure 7). This approach also eliminated inclusion of interior crater walls, except for the occasional case of recognizable valley networks in the interiors of large degraded basins. For basins that do contain mapped valleys the entire basin was analyzed, including tributaries not previously mapped.

[52] The local valley volume was measured by overlaying a 16×16 km box centered on a valley and calculating the valley volume from the detrended 75th percentile elevation as previously discussed. We utilized the 128 pixel/degree MOLA DEM with post-Noachian craters removed to measure valley volume. When this volume is divided by the box length it becomes a measure of valley cross-sectional area, A_V. Routing of eroded volume through the valley network starts at divides, and the first estimate of A_V was made when progressing downstream to a distance equal to half the box length (8 km). This approach then routed cumulatively downstream, multiplying A_V by cumulative distance to estimate V_T. To reduce the computational load, A_V was measured only at intervals equal to the box length, with the

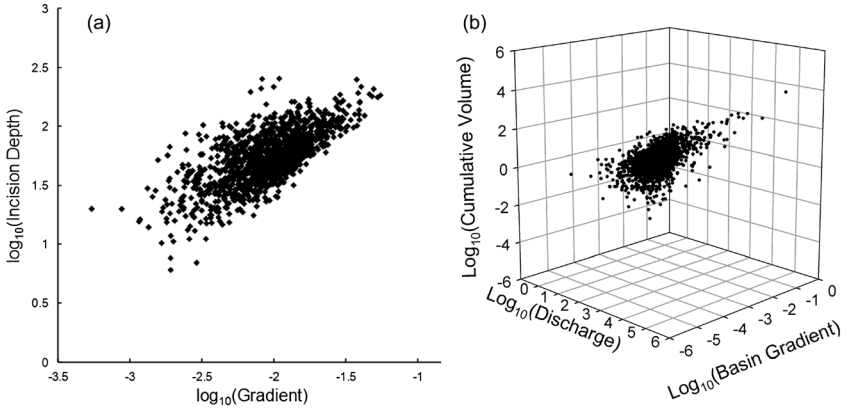

Figure 15. Example scatterplot relationships between variables. (a) Relationship between incision depth, I, and local valley gradient, S_V, for an assumed *X-ratio* of 2.7 and no flow attenuation. Plot is a random sampling of 1205 points from 1.2×10^4 sample reaches. (b) Relationship between estimated cumulative eroded valley volume, V_T, basin gradient, S_B, and local relative discharge, Q_F. This plot is for an *X-ratio* of 3.1, no flow attenuation, and relative elevation runoff exponent parameter $b = 0.00216$. Plot is a random sample of 2014 points from the 2.7×10^5 measurements.

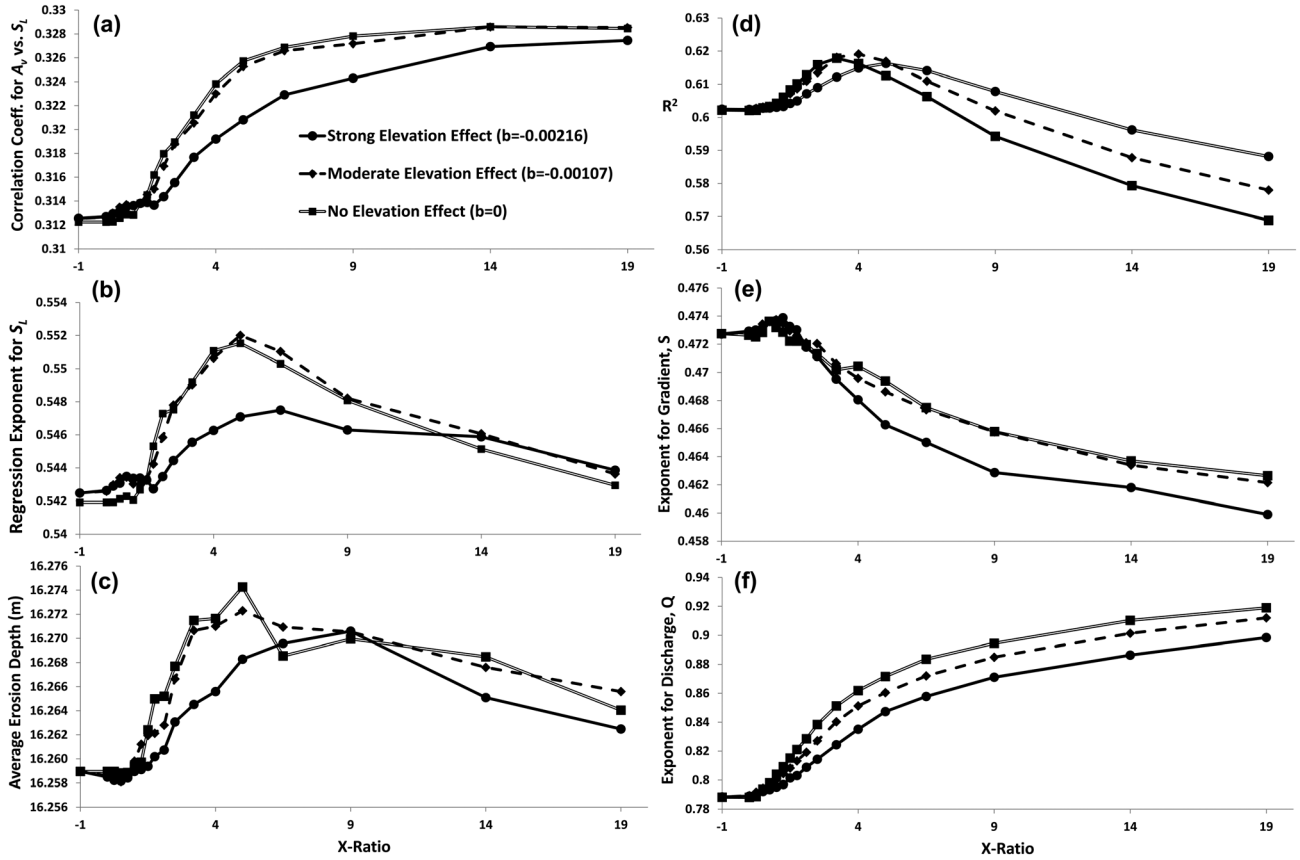

Figure 16. Plots of results for relationships for valley cross-sectional area and cumulative incision volume as a function of the modeled *X-ratio*. (a) Correlation coefficient in regression relationship between local values of valley cross-sectional area and local valley gradient. (b) The regression exponent for gradient for the same regression. (c) The estimated average local erosion depth as a function of the modeled *X-ratio*. (d) The R^2 value for a multiple regression estimating total cumulative erosion volume from the average upstream basin gradient and the modeled discharge. (e) The exponent for gradient in the multiple regression for cumulative erosion volume. (f) The exponent for discharge in the multiple regression for cumulative erosion volume. The multiple curves refer to simulations with different values of the degree of dependence of the *X-ratio* on relative elevation in equation (5).

assumption that A_V changes slowly downstream. Both A_V and V_T throughout the network are related to estimated flow, gradient, and basin topography in the analyses discussed below.

[53] Relative flood flows are routed through the drainage network with runoff volumes per unit land surface area that are either assumed to be spatially uniform or having elevation dependence (equation (5)). Routed flood flows terminate whenever flow enters a basin supporting a nonoverflowing lake. When flows enter a depression considered to host a "real" overflowing lake, the flow is attenuated as a function of the ratio of flood magnitude to lake area (equation (6)). Three different intensities of attenuation (K_A in equation (6)) were considered: no attenuation ($K_A = 0$), a moderate degree of attenuation ($K_A = 10$), and a high enough value of K_A (1000.0) that little flood discharge continued downstream of lake overflows. For each combination of assumed attenuation intensity and elevation dependency of precipitation, runoff, and evaporation flow routing, simulations were conducted for all 18 modeled values of mean *X-ratio*.

[54] Topographic gradients were measured in two ways. For examining the forcing of valley cross-sectional area A_V by valley gradient, the average topographic gradient, S_L, of a plane fit to elevations in the 16×16 km sample area was calculated. For relationships involving cumulative eroded volume, V_T, the average gradient of all local valley gradients within the upstream basin, S_B, was utilized.

5.3.1. Global Simulation

[55] Numerous regressions and correlations among estimated erosion volumes, estimated relative discharge, and valley gradients were conducted pooling observations from the entire cratered highlands excluding the floor of Hellas and Argyre, post-Noachian terrain, and regions south of 70°S (Figure 7). About 500,000 observations resulted for relating local values of variables, and 50,000 to 1,500,000 observations were obtained for routed eroded volume, depending on degree of flow attenuation. These regressions reveal the degree to which spatial patterns of cumulative valley volume are related to the likely controlling factors of discharge and basin gradient.

[56] Varying the degree to which precipitation varies with local relative elevation (parameter *b* in equation (5)) produced modest changes in estimated regression parameters. Changing the degree of flow attenuation in lakes (K_A in equation (6)) had negligible influence on estimated relationships between flow,

Table 3. Estimated Erosion Characteristics for Major Martian Valley Networks

			X-ratio = −1.0		*X-ratio* = 3.2					
Vallis/Valles or Location[a]	Longitude (°E)	Latitude (°)	Discharge (km^2)[b]	Eroded Volume (km^3)	Discharge (km^2)	Eroded Volume (km^3)	Discharge Ratio[c]	Volume Ratio[d]	Average Erosion Depth (m)[e] *X-ratio* = −1.0	Average Erosion Depth (m) *X-Ratio* = 3.2
Samara	337.38	−16.16	2,820,150	10,950	517,292	9,578	0.18	0.87	3.9	18.5
Loire	339.50	−16.25	364,191	2,414	187,905	1,898	0.52	0.79	6.6	10.1
Marikh	2.63	−15.44	2,134,580	3,507	77,520	2,239	0.04	0.64	1.6	28.9
Evros	4.50	−14.91	311,679	4,146	165,583	3,350	0.53	0.81	13.3	20.2
Verde	24.41	0.25	57,979	950	20,020	411	0.35	0.43	16.4	20.5
E of Dawes cr.	34.16	0.78	954,475	2,565	107,217	2,264	0.11	0.88	2.7	21.1
NE of Mosa v.	21.78	−13.19	56,108	866	20,848	402	0.37	0.46	15.4	19.3
Naktong	31.94	9.88	1,342,320	1,981	60,725	1,068	0.05	0.54	1.5	17.6
Naro	60.00	−2.03	95,795	737	52,174	674	0.54	0.91	7.7	12.9
Vichada	87.38	−23.06	23,420	901	18,781	827	0.80	0.92	38.5	44.0
Zarqa	82.09	1.78	203,051	6,338	100,683	6,056	0.50	0.96	31.2	60.1
E. of Zarqa v.	90.22	0.81	491,736	9,082	129,737	8,661	0.26	0.95	18.5	66.8
Tinto	110.84	−5.28	86,936	1,120	31,680	792	0.36	0.71	12.9	25.0
Tagus	113.28	−4.41	2,58,949	1,760	70,795	1,313	0.27	0.75	6.8	18.5
Licus	126.50	−1.97	153,618	5,117	89,211	3,979	0.58	0.78	33.3	44.6
Ma'adim	176.03	−18.06	6,228,510	11,332	126,943	10,639	0.02	0.94	1.8	83.8
Al-Qahira	164.41	−18.03	1,410,950	6,608	99,963	5,103	0.07	0.77	4.7	51.1
Durius	171.88	−17.81	202,472	5,037	75,856	4,236	0.37	0.84	24.9	55.8
near Slypher cr.	274.22	−46.78	138,799	1,727	120,286	1,652	0.87	0.96	12.4	13.7
Protva	304.72	−29.91	3,559,430	2,318	289,270	2,242	0.08	0.97	0.7	7.7
Parana	348.37	−24.18	139,374	2,964	86,618	2,401	0.62	0.81	21.3	27.7

[a]cr. = crater; v. = vallis/valles.
[b]Discharges were calculated in m^3 for a runoff depth of 1 m, so that discharges correspond to an effective drainage area ($m^3\ m^{-1}$), converted here to km^2.
[c]Ratio of discharge at *X-ratio* = 3.2 to discharge at *X-ratio* = −1.0.
[d]Ratio of estimated erosion volume at *X-ratio* = 3.2 to volume at *X-ratio* = −1.0.
[e]Ratio of eroded volume to effective drainage area.

erosion volume, and basin gradient, so we do not report these results.

[57] Local values of valley cross-sectional area (A_V), exhibit a moderate correlation with local gradient (S_L) with correlation coefficients in the range of 0.31 to 0.33 for all assumed *X-ratios*, elevation-dependency of local *X-ratios*, and intensity of flood attenuation (Figure 16a). The corresponding regression exponent for A_V dependency on S_L falls within the range of 0.54 to 0.55 (Figure 16b). Negligible correlations resulted, however, in relating A_V to local estimated flood discharge, local elevation, and latitude. The average erosion depth beneath the 75th percentile reference elevation among all sample locations generally increases as *X-ratio* decreases (Figure 16c), reflecting an increasing number of locations experiencing simulated flows. The average depth decreases, however for *X-ratios* less than about 4.0 as a result of submergence of some mapped valley segments.

[58] Cumulative valley volume (V_T) correlates strongly with local relative discharge, Q_F, and average basin gradient (S_B) with the corresponding correlation coefficients averaging about 0.78 and 0.21, respectively. A multiple regression of V_T on S_B and Q_F yielded R^2 values between 0.57 and 0.62, with the highest values for the lowest assumed *X-ratios* (Figure 16d). Figure 15b shows an example scatter plot of the relationship between V_T, S_B, and Q_F. Regression exponents for discharge generally fell between 0.78 and 0.92, with little dependency on assumed *X-ratio* (Figure 16f) but slightly higher values for large values of flow attenuation downstream from lakes. Exponents for S_B ranged between 0.46 and 0.47, with higher values with low intensity of downstream flow attenuation (Figure 16e).

[59] Simulation results for 21 major valley networks are summarized in Table 3. At the downstream end of each of these valleys the simulated discharge and the estimated total upstream valley volume is summarized for *X-ratios* of −1.0 and 3.2. Because the assumed runoff depth is 1.0 m, the discharge at $X = -1.0$ is proportional to the maximum possible upstream contributing area and for $X = 3.2$ the effective upstream area for that *X-ratio*. The effective contributing area diminishes markedly as the *X-ratio* increases, but the estimated erosion volume decreases less rapidly because most of the valley volume is concentrated along the higher-order valleys. The average erosion depth calculated for the maximum contributing area ($X = -1.0$) over all of the valleys is 17.1 m, nearly equal to the ~16.3 m value calculated for the entire Noachian highlands (Figure 16c). The average incision depth increases to 31.4 m for just the effective contributing area at $X = 3.2$.

5.3.2. Regional Simulation

[60] The degree of valley incision and its relationships to potentially controlling factors on a regional scale was examined by dividing the highlands of Mars into nonoverlapping square cells roughly 1066 km across at the equator. Cells for which more than 50% of its area fell outside of the inclusion mask (Figure 7) or did not contain more than 100 paired observations of A_V, Q_F, and S_L were not included in the analysis,. This approach resulted in 95 regional cells to be used. Figure 17a shows contours of mean cell elevation, H_C, for latitudes from 45°N to 70°S, with regions not considered in the analysis shown in white. For each cell, a plane was fit to DEM elevations within each cell and the regional slope (S_C, Figure 17b); the logarithm of the standard deviation of elevations relative to the fitted plane (Z_C, a measure of regional "roughness", Figure 17c) central cell latitude (ψ_C), and longitude (λ_C) were calculated.

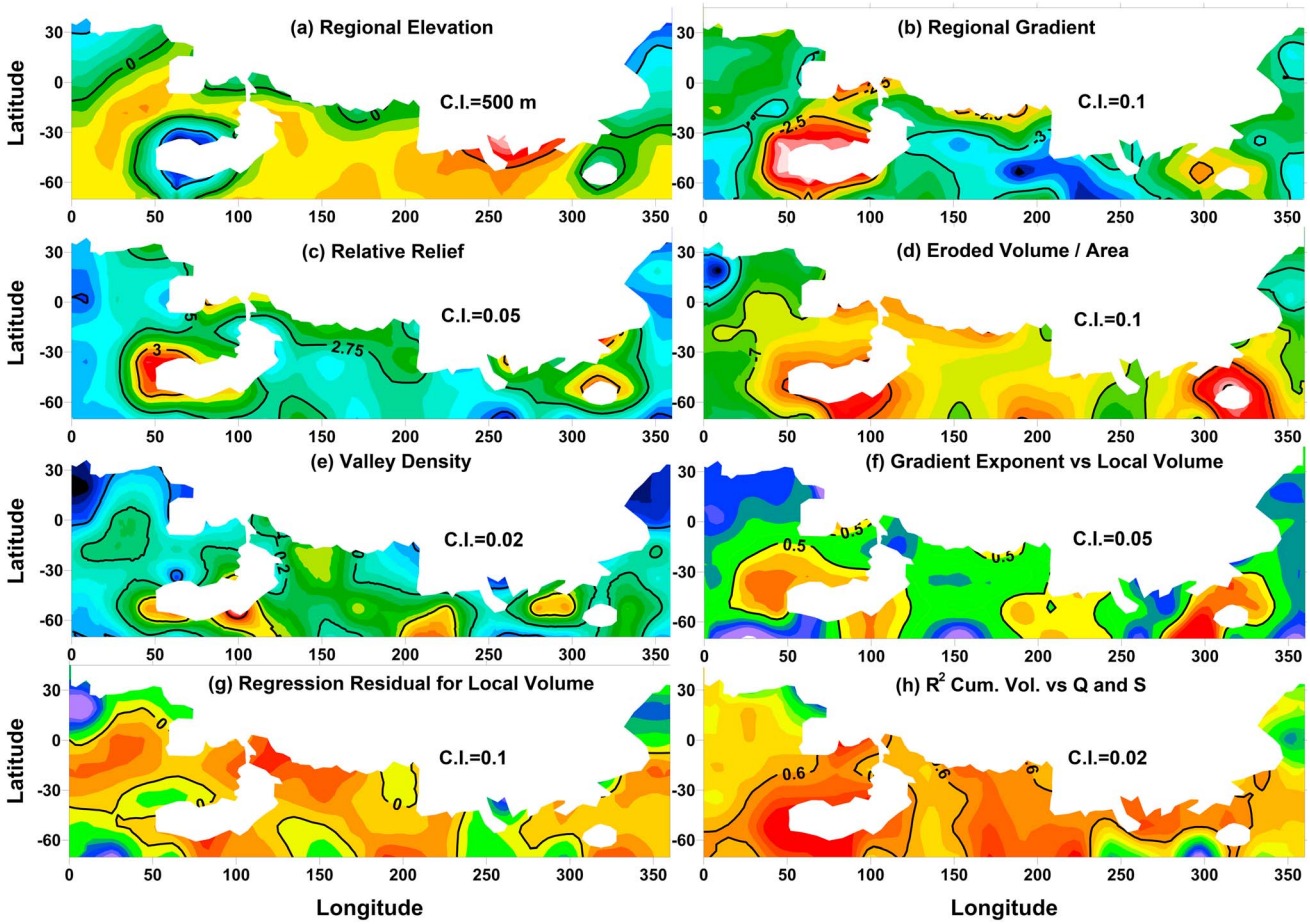

Figure 17. Spatial distribution of topographic properties and valley network statistics. (a) Mean elevation in regional 1066 × 1066 km cells covering the Martian highlands. (b) Gradient of a planar surface fit by least squares regression within each cells. (c) Mean square elevation variation (relative relief) around the elevations fit by the planar surface, expressed as the logarithm of the variation. (d) Estimated total eroded volume per unit area in valley networks. (e) Total length of mapped valley networks per unit area. (f) Exponent in a regression between local volume of erosion and the local valley gradient. (g) The unexplained residual from a multivariate regression of local volume on cell gradient, mean square elevation, and cell latitude. (h) Spatial variation of the regression R^2 value for a regression estimating cumulative eroded volume versus discharge and basin gradient. Fitted contours do not reflect the continuity across the 0°–360° meridian.

[61] Within each cell the average local values of valley cross-sectional area, $\bar{A}_V$, discharge, $\overline{Q}_F$, and local gradient, $\overline{S}_L$, were calculated, as was the average volume of valley erosion, $\overline{V}_T$, calculated as the sum of local valley cross-sectional areas times corresponding valley length divided by the cell area. Table 4 shows correlations between the above variables among the 95 regional cells for a single value of the global *X-ratio*, flood attenuation, and elevation dependence of local *X-ratio* that exhibits a high global correlation between $\overline{V}_T$, $\overline{Q}_F$, and $\overline{S}_L$ (*X-ratio* = 3.2, $b = 0.00216$). The values of these correlations do not vary appreciably with different choices of *X-ratio*, degree of flood attenuation, or elevation dependence of local *X-ratio*. In this Table only absolute values of correlations greater than 0.2 are shown, corresponding to a two-tailed 0.05 probability of incorrect assignment of statistical significance. Also included in the Table are the correlation coefficient, R_{VS}, and the regression exponent, N_{VS}, for log-linear regression of V_T on local gradient, S_L, for all data points within each of the 95 cells, and the equivalent regression coefficients for log-linear regression of V_T on discharge Q_F (R_{VQ} and M_{VQ}). Note that the entries for R_{VS}, N_{VS}, R_{VQ}, and M_{VQ} in Table 4 are the correlation coefficients *between* the 95 cells of the regression coefficients calculated *within* each of the cells. Finally, cell-averaged values of total valley length per unit cell area, D_D (a measure of drainage density), were also calculated.

[62] The relief properties among the cells in Table 4 show strong mutual correlations; Cell gradient, S_C, decreases with higher elevation, H_C, and S_C and relative relief, Z_C, correlate positively. The average valley cross-sectional area ($\bar{A}_V$), eroded volume ($\overline{V}_T$), and drainage density (D_D) correlate positively with cell gradient S_C and relative relief Z_C, as would be expected.

[63] Figure 17d shows the strong relationship between spatial variations in the eroded volume per unit area ($\overline{V}_T$) and regional gradient (S_C, Figure 17b) and relative relief (Z_C,

Table 4. Pairwise Correlation Coefficients Between Cell-Averaged Variables in Local Eroded Volume Analysis. Only Statistically Significant Correlations Are Shown.

	$\mathrm{Cos}(\Psi_C)$	H_C	S_C	Z_C	$\overline{V}_V$	$\overline{A}_V$	$\overline{S}_L$	$\overline{Q}_F$	R_{VS}	N_{VS}	R_{VQ}	M_{VQ}	D_D
H_C	−0.29	1											
S_C	0.25	−0.57	1										
Z_C		−0.30	0.63	1									
$\overline{V}_V$	−0.29		0.37	0.45	1								
$\overline{A}_V$		−0.30	0.43	0.46	0.41	1							
$\overline{S}_L$		−0.29	0.55	0.63	0.53	0.86	1						
$\overline{Q}_F$			0.46	0.39	0.72	0.26	0.44	1					
R_{VS}					0.41	0.36	0.31	0.26	1				
N_{VS}					0.45	0.26	0.27	0.29	0.96	1			
R_{VQ}				−0.25	−0.26	−0.29	−0.29		−0.50	−0.48	1		
M_{VQ}				−0.25		−0.29	−0.24		−0.47	−0.44	0.98	1	
D_D	−0.30			0.26	0.63			0.39	0.24	0.29			1

Figure 17c). The valley density (D_D, Figure 17e) generally shows the same positive relationship to relative relief and regional gradient. Both $\overline{V}_T$ and D_D exhibit strong positive values in a region centered at about 20°S and 25°E that does not correspond to very high regional relief or regional gradient. This area, sloping northwestward from the plateau surrounding Hellas, is located at the border between Noachis Terra and the southwestern extent of Margaritifer Terra and Arabia Terra, which has long been recognized as being strongly dissected [*Barnhart et al*., 2009; *Grant*, 2000; *Grant and Parker*, 2001; *Hynek and Phillips*, 2001]. This is also in the area where lakes overflowed at relatively high *X-ratio* values [*Matsubara et al*., 2011]. Valley density (D_D) also has local high valleys near 50°S 200°E and 50°S 280°E in regions not having strong local relief or regional gradients. These likewise correspond to areas where lakes readily overflowed at relatively high *X-ratio* values [*Matsubara et al*., 2011].

[64] The exponent for gradient, N_{VS}, in a regression of local eroded volume versus gradient correlates positively with regional gradient (S_C) and local relief (Z_C) (Table 4 and Figure 17f). The correlation coefficient for this regression R_{VS} also exhibits the same pattern (Table 4).

[65] The residual from a multivariate regression of local volume ($\overline{V}_T$) on regional gradient (S_C), relative relief (Z_C), and latitude $Cos(\psi_C)$ explains 55% of the spatial variation of $\overline{V}_T$ (Figure 17g). Strong positive residuals (high relative erosion volumes) occur in the region centered at about 20°S and 25°E discussed above, plus locations near the highlands-lowlands boundary between 50°E and 230°E, a region south of Hellas (60°S between 30–120°E) and 40–60°S, 170–210°E.

[66] The spatial pattern of the cell morphometric variables was examined for a multiple regression involving cumulative volume (V_F) against Q_F and basin gradient (S_B) within each cell, as expressed in the regression R^2_{VQS}, the exponents M_{VQ} and N_{VS}, and the intercept C_{VQS} (Table 5). A similar multiple regression relating S_B to V_T and Q_F within regional cells (regression coefficients R^2_{SQV}, M_{SQ}, T_{SV}, and C_{VQS}) was also examined (Table 5). Consistent variation seen in measures of intensity of valley incision between nearby cells presumably expresses corresponding spatial variability of forcing factors such as relief properties and simulated discharge. The strength of the multiple regression estimating cumulative volume by basin gradient and discharge (R^2_{VQS}) is strongest in cells with high regional gradient and high region relief (Table 5). A similar pattern occurs for the multiple regression estimation of gradient by cumulative volume and discharge (Table 5 and Figure 17h).

6. Discussion

6.1. Comparison With Theoretical Models of Valley Incision

[67] The long-term erosion of valley networks functionally depends upon the nature of the channel bed, available relief, and discharges of water and sediment. In this section we examine the results of our analysis of the patterns and controlling factors of valley incision in relationship to theoretical expectations for different classes of valley types.

Table 5. Multiple Regression Coefficients Between Cell-Averaged Variables in Cumulative Eroded Volume Analysis. Only Statistically Significant Correlations Are Shown.

	$\mathrm{Cos}(\Psi_C)$	H_C	S_c	Z_C	R^2_{VQS}	M_{VQ}	N_{VS}	C_{VQS}	R^2_{SQV}	M_{SQ}	T_{SV}
H_C		1									
S_C		−0.25	1								
Z_C			0.67	1							
R^2_{VQS}			0.28	0.32	1						
M_{VQ}					0.81	1					
N_{VS}				0.31	0.42	0.37	1				
C_{VQS}	−0.45						0.85	1			
R^2_{SQV}			0.33	0.33	0.41	0.29	0.87	0.76	1		
M_{SQ}	029				−0.54	−0.42	−0.85	−0.75	−0.88	1	
T_{SV}			0.26	0.26	0.45	0.32	0.86	0.73	0.94	−0.90	1
C_{SQV}			0.49	0.49	0.47	0.42	0.69	0.64	0.72	−0.77	0.70

6.1.1. Bedrock vs. Alluvial Channels

[68] The spatial pattern of valley incision and how it relates to surface gradient and flow magnitudes should depend on the nature of the channel occupying the valley, specifically whether the channel is bedrock-floored or has a covering of alluvium [*Howard*, 1980; *Howard et al*., 1994]. In the former the rate of channel incision is related to flow discharge, channel gradient, and in many cases to abrasion of the bed by sediment in transport. Incision of alluvial channels depends on the stream transport capacity, which in turn is a function of discharge, stream gradient, and sediment size.

[69] In many terrestrial stream systems the primary agent of channel bed erosion is impact abrasion by sediment in transport. The rate of bed erosion functionally depends in a complicated manner on the strength of the channel bed, the quantity and size of sediment in transport, the fractional coverage of the bed by sediment, and flow intensity [*Sklar and Dietrich*, 2001, 2004a, 2004b]. When the bedload transport rate is low, the bed coverage by sediment is minimal. The quantity of sediment in transport largely correlates with contributing area (and discharge) and as a consequence the amount of erosion should functionally depend on discharge and gradient as expressed by equation (7).

[70] Within alluvial-floored channels, sediment transport rates can still be expressed as a power function of discharge and channel gradient, although with different exponents than those in equation (7) [e.g., *Howard*, 1994]. If discharges vary systematically through a drainage network, then the total long-term erosion measured by total eroded volume might correlate with discharge and basin gradient in a functional relationship similar to equation (7).

[71] In the succeeding sections we compare the results of our analysis with what relationships should be expected if the channels were bedrock versus alluvial channels, including whether they have coarse- or fine-grained beds.

6.1.2. Bedrock Channels

[72] If a drainage basin is undergoing long-continued erosion in a bedrock channel basin within uniform lithology, the rate of erosion tends toward spatial uniformity, and gradient and discharge have a strong inverse relationship (implying a concave downstream profile) [*Howard*, 1998; *Whipple and Tucker*, 1999]. Thus, incision depth or valley cross-sectional area should not have a strong correlation with either discharge or gradient. On the other hand, if a drainage network has incised shallowly into an irregular initial topography (such as is produced by impact cratering), then the observed rate of incision should correlate with both discharge and local gradient (equation (7)) in such a transient network.

[73] Theoretically driven values for m and n for stream power dependent erosion of bedrock are about 0.3 and 0.7, respectively (equation (7)) [*Howard and Kerby*, 1983; *Howard*, 1994]. These exponents express relative effects of discharge and slope, respectively, on valley incision within the stream network. While the observed value for n (0.57) in estimating incision depth matches reasonably well with the theoretical value, the estimated m value (0.03) is an order of magnitude smaller than expected. A similar result was obtained for the regression relating valley cross-sectional area, A_V, to valley gradient, S_L, with an exponent of about 0.54 (Figure 16b). The power-law regression of A_V against estimated Q_F yielded consistently low correlations and estimated exponents for Q_F well below those expected for stream power bedrock erosion. Discharge is largely a measure of upstream contributing area (with the complication of evaporation and flood attenuation in Martian lakes), so that a small value of the m exponent implies incision depths do not systematically increase downstream in Martian fluvial networks as strongly as would be expected in steady state bedrock valley networks. On the other hand, a small estimated discharge exponent with a large gradient exponent could be consistent with transient erosion of bedrock channels.

[74] If the valleys were bedrock-floored but eroded by bedload sediment abrasion [*Sklar and Dietrich*, 2001, 2004b, 2006], then total erosion and valley cross-sectional area, A_V, should correlate with the sediment flux through the valley as estimated by the total cumulative eroded volume, V_T. A modest (~0.2) correlation does exist between A_V and V_T, but this correlation is not high enough to be conclusive. The dependency of erosion rate on gradient in the *Sklar and Dietrich* [2001, 2004b, 2006] model is inverse rather than the observed positive correlation, but the *Chatanantavet et al*. [2010] flux-dependent bedrock erosion model suggests a positive relationship with gradient.

6.1.3. Threshold Alluvial Channels

[75] If the valley networks on early Mars were floored with coarse alluvium at the threshold of motion, then the local gradient should be a positive function of grain size (exponent of 0.9 to 1.4) and an inverse function of discharge (exponent of –0.34 to –0.43) [*Howard*, 1980]. The observed relationship between local gradient and estimated discharge is modest, with a negative exponent only for small *X-ratios*. Because the alluvial grain size in Martian valleys cannot be measured with available data, the role of grain size in setting valley gradients cannot be assessed. In terrestrial stream networks the grain size of coarse-bed channels often varies significantly within drainage basins, often coarsening (and steepening the channel) where slope processes deliver coarse debris or at sites of entrance of debris flows from steep tributaries [*Hack*, 1972; *Howard and Dolan*, 1981; *Howard*, 1980, 1998; *Pizzuto*, 1992]. These local grain size effects on gradient might obscure the role of flood magnitude in controlling valley gradients.

6.1.4. High Sediment Discharge Alluvial Channels

[76] In alluvial channels carrying appreciable quantities of bedload (generally limited to sand or fine gravel bed channels) the channel gradient at equilibrium should be related in a positive power law relationship with quantity of sediment load and a negative relationship to discharge. In an eroding valley network the long-term sediment flux should be proportional to the cumulative upstream erosion, V_T. Multiple regression of local valley gradient, S_L, as a power function of estimated flood discharge, Q_F, and cumulative valley volume, V_T, show the expected positive exponent for V_T and a negative exponent for Q_F, but the exponents are smaller than the theoretically driven values, and the explained variance is small ($R^2 \sim 0.1$).

6.1.5. Conclusions Regarding Channel Bed Type

[77] In both bedrock and alluvial channel systems the total volume of erosion should be a positive function of valley gradient and available discharge. We tested this expectation through a regression of cumulative valley volume, V_T, in a power function relationship to estimated flood discharge, Q_F, and basin gradient, S_B, across all valley systems. This

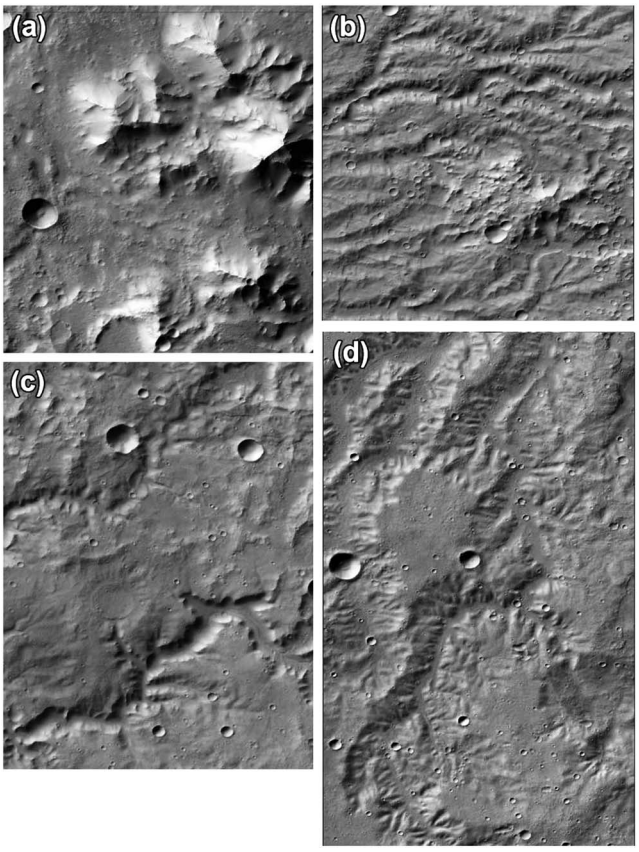

Figure 18. Representative images of incised valley networks. All images are about 26.5 km across and are unprojected, with north toward top. Figures 18a and 18b show regions where dissection is deep enough (mountainous area in Figure 18a) that the original surface prior to incision is not preserved in divides. Figures 18c and 18d show the more usual situation where the valley networks are sharply incised into remnant upland surfaces. (a) Part of CTX image B20_017392_1776, centered at 92.64°E, 3.91°. (b) Part of CTX image P21_009049_1580, centered at 349.2°E, 20.47°S. (c) Part of CTX image B20_017409_1562, centered at 350.60°E, 22.41°S. (d) Part of CTX image 20_017554_1545, centered at 352.88°E, 27.13°S.

relationship has high explanatory power (R^2 of 0.57 – 0.62) (Figure 16d), with exponents for Q_F ~0.9 (Figure 16f) and for basin gradient S_B ~0.47 (Figure 16e). Because both Q_F and V_T are accumulated downstream, a positive relationship is almost inevitable. However, the strength of the relationship of volume to both gradient and discharge is indicative that the Martian valley networks were highly integrated with distributed sources of discharge, long flow paths, and erosion and sediment transport distributed through the networks.

[78] The Martian highlands are densely cratered, thus a highly fractured megaregolith would be expected, transitioning downward into more indurated bedrock [e.g., *Clifford*, 1993; *Melosh*, 1989]. Because Martian valleys are typically incised 50 to more than 300 m, erosion may slow down upon reaching indurated rock so that there would not be a systematic downstream increase in erosion depth. However, incision depths are strongly correlated with valley gradient, which would not be expected if a resistant horizon at depth inhibits erosion.

[79] The Martian valley networks likely were a mixture of bedrock and alluvial channel segments. A channel can start, for example, as a bedrock channel near the head waters and transition to an alluvial channel near the downstream end. Moreover, in many regions terrestrial stream channels exhibit a thin or discontinuous mantling of sediment over bedrock (mixed bedrock-alluvial channels) [e.g., *Howard*, 1998]. The distinction between bedrock versus alluvial channels in ancient channels seen in satellite images is difficult due to lack of resolution and degradation of valley floors by surface processes such as aeolian sedimentation, mass wasting, cratering, and weathering. If a significant fraction of Martian valleys were alluvial, then the observed lack of a strong relationship between incision depth (or valley cross-sectional area) and estimated discharge could be expected. Samara Valles (Figure 9a) exhibits a smooth, concave profile with a low gradient in the downstream portion ($S \sim 0.001$), consistent with an alluvial valley. A representative valley on the Isidis basin southern interior rim has a stepped longitudinal profile, with steep segments ($S \sim 0.03$) where it cuts through massifs of the Isidis rim, and gentler intervening sections ($S \sim 0.005$), suggesting alluvial reaches graded to intervening steeper bedrock or boulder reaches (Figure 9b). A number of studies have remarked on the irregular profiles of valley networks [e.g., *Aharonson et al*., 2002; *Howard et al*., 2005; *Kereszturi*, 2005; *Penido et al*., 2013] indicating the immaturity of erosion on Mars; this irregularity is likely to be associated with different bed types in different reaches. Many valley networks terminate in presumed depositional basins, and are thus likely to be alluvial in their lower reaches. Because alluvial channels are graded to their controlling base level (a depositional basin or a downstream bedrock reach) and in such situations channels can aggrade rather than erode as basins become infilled causing incision depths to not necessarily correlate with estimated discharge. However, in alluvial valley systems, cumulative total erosion V_T would be expected to correlate with downstream increase in discharge, Q_F, as is observed (Figure 15b).

6.2. Volume of Erosion

[80] Our measurements of incision depth and eroded volume of the classic valley networks dating to the Noachian-Hesperian transition comprise a small, but poorly quantified fraction of the total amount of fluvial erosion occurring during the Noachian. For example, the deeply incised part of the Samara Valles system does not include a broad trough that surrounds the incised valley (e.g., in the upper left of Figure 10a above "&"). This trough is likely an ancestral counterpart to the incised Samara Valles. The high degree of drainage integration of the Samara, Parana, and Loire Valles systems indeed requires that extensive fluvial erosion had to precede the final stage of valley incision, because surface drainage paths on a saturated cratered surface are very short. Depositional processes such as airfall deposition and lava infilling and purely mass wasting processes could not have created the requisite long flow paths [*Craddock and Howard*, 2002; *Howard et al*., 2005; *Howard*, 2007; *Irwin et al*., 2008, 2011]. Many deeply eroded and deeply infilled large basins occur on the Martian highlands that predate the valley incision, such as the Parana Basin ("#" in Figure 10a) and the depression "&" in Figure 10a. Fluvial processes

probably dominated such basin degradation [*Forsberg-Taylor et al*., 2004].

6.3. Model Limitations

[81] The model does not account for any systematic spatial variation of runoff due to substrate properties. Impact regolith would encourage infiltration and evaporation from soil moisture rather than runoff and this may cause watersheds to generate overland flow from only limited parts of the catchment area weakening the relationship between discharge and the catchment area. Infiltration losses are implicitly accounted for in the closed basin system because the water lost to groundwater would eventually feed into a lake downstream but this would lower the dominant discharge for the upstream region. This process also means that if discharge is dominantly fed by local groundwater, exfiltration flood peaks are diminished, also weakening the relationship between the discharge and catchment area. Other influences that may cause spatial variation in discharge that are not directly related to elevation, such as infiltration rate of the substrate materials, are not included in the analysis because of lack of appropriate data, but they may have influenced the pattern of regional discharges.

[82] The assumptions we made in estimating incision depth may be erroneous in some locations. In most places valleys are eroded into a relatively gentle upland surface that largely remains at its original elevation [*Carr*, 2012; *Howard et al*., 2005] (Figures 18c and 18d). While this assumption allows us to measure incision as the difference in elevation between the valley floor and the upland surface, the erosion depth estimation becomes questionable in mountainous regions where an initial surface may not be preserved due to deep incision (Figures 19a and 19b). In such locations the use of a specific value of the relative relief (e.g., the 75th percentile) may simply be measuring local relief rather than an incision depth.

[83] This issue was addressed by using a discriminant function analysis of the hypsometric properties of valleys to distinguish between deeply eroded landscapes and valleys incised into upland surfaces. Valley networks in eight terrestrial networks (Australia, Colorado, Wisconsin, West Virginia, Taiwan, New Zealand, and Africa) were digitized and classified into three categories: valleys clearly incised into a low-relief uplands surface (incised landscapes, e.g., Figure 18b), mountainous high relief valleys lacking an identifiable upland surface (Figure 18a), and transitional reaches left unclassified. Various parameters were used as independent variables to define discriminant functions separating incised versus high-relief landscapes. The resulting function was able to correctly classify 88% of the incised valleys and 91% of the high relief valleys. This function was used to further eliminate selected Martian valley reaches so that only incised valleys are used for further analysis. This restriction of the database to valleys showing an incised character did not, however, change the resulting m, n, and K values ("Discriminant Function" in Table 2).

[84] Another issue that may affect the estimation of effective discharge is the presence of crater lakes along the valleys. Although modeling of flood attenuation caused by lakes resulted in m and n estimated values similar to those without a flood attenuation effect, catastrophic overflow and breaching of natural lakes can likewise cause catastrophic erosion, similar to what happens in dam breaks. This flooding has an opposite effect from the attenuation discussed above, and deep valley incision can occur in a short period of time. Overflow of paleolake Bonneville is one terrestrial example of such an outflow erosion event [*Oviatt*, 1997]. It has been suggested that Ma'adim Valles on Mars has also formed from such a catastrophic outflow [*Irwin et al*., 2002, 2004].

6.4. Climate Associated With Valley Network Formation

[85] The constraints that our analysis place on the hydrology of Mars during the epoch of valley network incision permits a wide range of possible associated climate regimes. The widespread occurrence of the valley networks, the occurrence of overflowing lakes, the impressive volumes of surficial deposits eroded and deposited during valley incision, and many other forms of evidences indicate that the water flowing through the valley networks was runoff from precipitation (snow/rain) [*Carr*, 2012; *Craddock and Howard*, 2002; *Fassett and Head*, 2008b; *Grant*, 2000; *Howard et al*., 2005; *Hynek and Phillips*, 2001; *Hynek et al*., 2010; *Irwin et al*., 2008]. The dimensions of channels locally exposed within the valley networks indicate substantial discharges (about equal to the mean annual floods within terrestrial drainage networks of comparable drainage area) occurred at least occasionally [*Irwin et al*., 2005a, 2008; *Jaumann et al*., 2005]. Occasional discharges of this magnitude were also probably required to transport and comminute gravels and boulders that would inevitably have been introduced into eroding valley networks from megaregolith containing coarse ejecta blocks, fragmented lava flows and other coarse debris [*Hoke et al*., 2011].

[86] A climatic scenario most comparable to Earth would be evaporation from lakes or oceans precipitated as rain or snow, and resulted in runoff associated with the annual seasonal cycle, probably modulated by the large quasi-cyclical orbital variations experienced by Mars [*Laskar et al*., 2004]. Within that framework there are a wide variety of possible analog climates, including hot and cold deserts, and alpine and periglacial regimes that could generate the range of aridity indices (*X-ratios*) that is suggested by our hydrological analyses.

[87] We have noted above, however, the difficulties faced in finding mechanisms that would have generated a climate substantially warmer than Mars' present conditions, particularly for conditions warm enough for precipitation as rain. This is a problem also faced in explaining Earth's early warm climate [*Feulner*, 2012]. This issue has led to suggestions that Mars might never have had a climate with substantial time periods above freezing, but rather one in which snow and ice might have accumulated in the highlands seasonally or over long periods of time and released by surface or basal melting either seasonally, during rare extreme orbital configurations, or episodes of warming from release of greenhouse gasses [*Carr and Head*, 2003; *Fastook et al*., 2012; *Kite et al*., 2011, 2013]. If snow and ice accumulated as relatively thin blankets and then episodically melted under cold-based conditions, the climate and resulting landforms would resemble terrestrial alpine and high-latitude landscapes but without glacial features; such a scenario would probably be consistent with observed equatorial morphology. Accumulations of ice and snow reaching several hundreds of meters in thickness resulting in basal melting [*Carr and Head*,

2003] is quantitatively insufficient to produce the large discharges necessary for valley excavation (M. H. Carr, 2011, personal communication) and would produce a suite of landforms (eskers, tunnel valleys, glacial flow, and scour) not observed in the Noachian equatorial landscapes. Episodic surficial melting of thick, cold-based snow and ice accumulations (which climate simulations suggest might occur on an early Mars not quite warm enough to produce seasonal melting [*Forget et al*., 2013; *Wordsworth et al*., 2013] probably would not produce the pattern of fluvial sculpting of crater walls and the radial bajada infilling of Noachian craters that characterize the Martian highlands.

7. Conclusions

[88] We find that incision depths and valley cross-sectional areas are strongly influenced by valley gradient ($n \sim 0.57$ in equation (7)) but weakly related to modeled flood discharge ($m \sim 0.03$) with a multiple regression R^2 of about 0.44. The low estimated dependency of erosion depth and valley cross-sectional area on discharge, despite taking into consideration the effects of flood attenuation, orographic effect on precipitation, and discriminant analysis of valley hypsometry, may indicate that many channel segments on Mars were alluvial or mixed alluvial-bedrock channels rather than entirely bedrock-floored. Strong multiple correlations occur between the cumulative downstream volume of erosion versus gradient and estimated discharge. This relationship would be expected in both alluvial and bedrock valley systems. The mechanics of fluvial channels depends strongly upon the nature of the bed, whether bedrock, sand, or gravel [e.g., *Howard*, 1980]. To properly assess the relationship between incision depth and discharge, channel types must be identified for each valley. Unfortunately, because of the significant degradation of valleys by impacts, aeolian infilling of valleys, mass-wasting, and fretting processes, the original nature of valley networks is generally unobservable, except very locally [e.g., *Irwin et al*., 2005a]. Moreover, even where channel beds are exposed, only boulders larger than about 1 m in size would be visible in the highest resolution (HiRISE) images. Thus, we are not able to strongly constrain the types of channels characterizing individual portions of the valley network, but it is likely that all of the bed types coexisted when the valley networks were active.

[89] Regional analysis shows that average incision depths and eroded valley volume correlate strongly with gradient and relief, as would be expected within fluvial networks [e.g., *Barnhart et al*., 2009; *Irwin et al*., 2011] (Tables 4 and 5). Residuals from a regional regression of average valley volume on latitude, local relief, and regional gradient show a few regions with large positive residuals (Figure 17g), possibly indicating locally enhanced precipitation. One such region is within 10°S to 25°S and 330°W to 40°E on the strong NW regional gradient on the exterior slope of the Hellas Basin. Strong positive residuals also occur on the steep regional slopes south of the boundary between the northern lowlands and southern highlands between 80°E to 200°E. Estimated average erosion depth within the highlands region during the epoch of valley network formation is about 17 m.

[90] We found that flow simulations with a strong dependency of runoff rates upon relative elevation delivered larger amounts of water to the downstream portions of drainage networks for the same average *X-ratio* (Figure 12). Strong orographic effects on precipitation would imply atmospheric pressures of a substantial fraction of 1 bar [*Wordsworth et al*., 2011, 2013].

[91] Our analysis places few constraints on the magnitude and frequency of the flows excavating the valley networks. Our analysis is based on relative rather than absolute values of discharge. Analysis of width and meander wavelength of locally visible channels within the valley networks suggests effective discharges about equal to the mean annual flood in terrestrial stream systems having the same contributing area [*Irwin et al*., 2005a; *Jaumann et al*., 2005]. Similarly, determining the duration of valley-excavating flows requires additional assumptions about bed sediment grain size, bed type (alluvial or bedrock), and flow frequencies (e.g., continuous, annual, or epochal), that such analyses can only address the minimum time scales for valley excavation [*Hoke et al*., 2011; *Jerolmack et al*., 2004; *Moore et al*., 2003].

[92] Regression models relating measures of valley network incision to terrain gradient and estimated discharge were utilized to make predictions about climatic conditions required to incise valley networks that we see on Mars. Our simple analysis of the *X-ratio* at which appreciable discharges would have occurred within representative valley networks provides the most definitive constraint on possible Martian paleoclimate while our other analysis methods show a weak dependency of incision depths and valley volumes upon the assumed *X-ratio*. Nonetheless, our valley incision/discharge analyses point to the necessity for climatic conditions on early Mars at least as moist in terms of the balance of runoff and lake evaporation as occurred in the Great Basin region of the U.S. during the late Pleistocene when large lakes were present, with estimated *X-ratios* in the range of 1 to 4. This optimum *X-ratio* range is comparable to that predicted from our earlier lake basin analysis (*X-ratio* range of 3 to 7) [*Matsubara et al*., 2011]. These low *X-ratios* imply an appreciable inventory of surface water in crater and intercrater basins, high water tables, and high runoff potential from lakes and saturated lowlands. This climate would have had to be maintained for hundreds and most likely many thousands of years to create the observed valley networks, many of which extend for thousands of kilometers with extensive tributary systems.

Notation

[93] This list includes the main variables, model parameters, and table entries.

A_V	Valley cross-sectional area
$\bar{A}_V$	Average valley cross-sectional area in regional cell (Table 4)
b	Coefficient for elevation-dependency of *X-ratio* (equation (5))
D_D	Drainage density in regional cell (Table 4)
E	Yearly depth of evaporation from lakes (equation (1))
H_C	Regional cell mean elevation (Tables 4 and 5)
H_R	Local relative elevation (equation (5))
M_{VQ}	Exponent for Q_F in multiple regression of V_T against Q_F and S_L within regional cell (Table 5)
N_{VS}	Exponent for S_L in multiple regression of V_T against S_L and Q_F within regional cell (Table 5)

M_{SQ} Exponent for Q_F in multiple regression of S_L against V_T and Q_F within regional cell (Table 5)
T_{SV} Exponent for V_T in multiple regression of S_L against V_T and Q_F within regional cell (Table 5)
I Local incision depth (equation (7))
C_{VQS} Intercept in multiple regression of V_T against Q_F and S_L within regional cell (Table 5)
C_{SQV} Intercept in multiple regression of S_L against Q_F and V_T within regional cell (Table 5)
K Constant in regression of I against Q_F and S_V (equation (7) and Table 2)
K_A Flow attenuation coefficient (equation (6))
m Exponent for Q_F in regression of I against Q_F and S_V (equation (7) and Table 2)
M_{VQ} Exponent in regression of V_T against Q_F within regional cell (Table 4)
n Exponent for S_V in regression of I against Q_F and S_V within regional cell (equation (7) and Table 2)
N_{VS} Exponent in regression of V_T against S_L within regional cell (Table 4)
Q_F Local estimated flood discharge (equation (7))
$\overline{Q_F}$ Average estimated flood discharge in regional cell (Table 1)
R_C Critical ratio of influent mean annual discharge to lake area (equation (6))
R_{VS} Correlation coefficient in regression between V_T and S_L within regional cell (Table 4)
R_{VQ} Correlation coefficient in regression between V_T and Q_F within regional cell (Table 4)
R^2_{SQV} Regression R^2 value for regression of S_L against Q_F and V_T within regional cell (Table 5)
R^2_{VQS} Regression R^2 value for regression of V_T against Q_F and S_L within regional cell (Table 5)
S_B Upstream basin gradient
S_C Topographic gradient of regional cell
S_L Local topographic gradient
$\overline{S_L}$ Average value of local gradient in regional cell
S_V Local valley gradient (equation (7))
V_I Yearly volumetric inflow to a basin (equation (1))
V_O Yearly volumetric outflow from a basin (equation (1))
V_T Cumulative eroded volume
$\overline{V_T}$ Average volume of eroded volume in regional cell
X The *X-ratio* (equation (2))
Z_C Roughness of regional cell (Tables 4 and 5)
λ_C Longitude of regional cell center
ψ_C Latitude of regional cell center (Tables 4 and 5)

[94] **Acknowledgments.** We thank Rossman Irwin, Robert Craddock, Sharon Wilson, Jeffery Moore, and Daniel Hobley, who made invaluable comments on a draft version of this manuscript. The manuscript was also improved by review comments by Caleb Fassett and an anonymous reviewer. This research was supported by NASA Planetary Geology and Geophysics grant.

References

Aharonson, O. et al. (2002), Drainage basins and channel incision on Mars, *Proc. Natl. Acad. Sci. U.S.A.*, *99*(4), 1780–1783.

Barnhart, C. J., et al. (2009), Long-term precipitation and late-stage valley network formation: Landform simulations of Parana Basin, Mars, *J. Geophys. Res.*, *114*, E01003, doi:10.1029/2008JE003122.

Basha, H. A. (1994), Nonlinear reservoir routing - Particular analytical solution, *J. Hydraul. Eng. ASCE*, *120*(5), 624–632.

Budyko, M. I. (1974), *Climate and Life*, p. 508, Academic, San Diego, Calif.

Burr, D. M. et al. (2009), Pervasive aqueous paleoflow features in the Aeolis/Zephyria Plana Region, Mars, *Icarus*, *200*, 52–76.

Carr, M. H. (2012), The fluvial history of Mars, *Philos. Trans. R. Soc. Lond. A*, *370*, 2193–2215.

Carr, M. H., and J. W. I. Head (2003), Basal melting of snow on early Mars: A possible origin of some valley networks, *Geophys. Res. Lett.*, *30*(24), 2245, doi:10.1029/2003GL018575.

Chatanantavet, P., et al. (2010), Physically based model of downstream fining in bedrock streams with lateral input, *Water Resour. Res.*, *46*, W02518, doi:10.1029/2008WR007208.

Clifford, S. M. (1993), A Model for the Hydrologic and Climatic Behavior of Water on Mars, *J. Geophys. Res.*, *98*(E6), 10973–11016.

Craddock, R. A., and A. D. Howard (2002), The case for precipitation on a warm, wet early Mars, *J. Geophys. Res.*, *107*(E11), doi:10.1029/2001JE001505.

Fassett, C. I., and J. W. Head (2008a), Open-Basin Lakes on Mars: Implications of Valley Network Lakes for the Nature of Noachian Hydrology, paper presented at Lunar and Planetary Institute Conference Abstracts, March 1, 2008.

Fassett, C. I., and J. W. I. Head (2008b), Valley network-fed, open-basin lakes on Mars: Distribution and implications for Noachian surface and subsurace hydrology, *Icarus*, *198*, 37–56, doi:10.1016/j.icarus.2008.1006.1016.

Fastook, J. L. et al. (2012), Early Mars climate near the Noachian-Hesperian boundary: Independent evidence for cold conditions from basal melting of the south polar ice sheet (Dorsa Argentina Formation) and implications for valley network formation, *Icarus*, *219*, 25–40.

Feulner, G. (2012), The faint young sun problem, *Rev. Geophys.*, *50*, RG2006, doi:10.1029/2011RG000375.

Forget, F. et al. (2013), 3D modelling of the early martian climate under a denser CO2 atmosphere: Temperatures and CO2 ice clouds, *Icarus*, *222*, 81–99.

Forsberg-Taylor, N. K., et al. (2004), Crater degradation in the Martian highlands: Morphometric analysis in the Sinus Sabaeus region and simulation modeling suggest fluvial processes, *J. Geophys. Res.*, *109*, E05002, doi:10.1029/2004JE002242.

Grant, J. A. (2000), Valley formation in Margaritifer Sinus, Mars, by precipitation- recharged ground-water sapping, *Geology*, *28*(3), 223–226.

Grant, J. A., and C. M. Fortezzo (2005), New insights into the geologic history of Margaritifer Sinus and discovery of a phreatomagmatic event during late-stage fluvial activity, Lunar Planet Sci. Conf. XXXVI, Abstract 1439.

Grant, J. A., and T. J. Parker (2001), The History of Water Discharge in the Margaritifer Sinus Region of Mars, paper presented at Lunar and Planetary Science Conference, March 1, 2001.

Hack, J. T. (1972), Studies of Longitudinal Stream Profiles in Virginia and Maryland, *U. S. Geol. Survey Prof. Paper 294-B*, 45–97.

Hoke, M. R. T. et al. (2011), Formation timescale of large Martian valley networks, *Earth Planet. Sci. Lett.*, *312*, 1–12.

Horn, D. R. (1987), Graphic estimation of peak flow reduction in reservoirs, *J. Hydraul. Eng. ASCE*, *113*(11), 1441–1450.

Howard, A. D. (1980), Thresholds in river regimes, in *Thresholds in geomorphology*, edited by D. R. Coates and J. D. Vitek, pp. 227–258, George Allen & Unwin, London.

Howard, A. D. (1994), A Detachment-Limited Model of Drainage-Basin Evolution, *Water Resour. Res.*, *30*(7), 2261–2285.

Howard, A. D. (1998), Long profile development of bedrock channels: Interaction of weathering, mass wasting, bed erosion and sediment transport, in *Rivers over Rock, Geophysical Monograph 107*, edited by E. Wohl and K. Tinkler, pp. 297–319, American Geophysical Union, Washington, D.C.

Howard, A. D. (2007), Simulating the development of martian highland landscapes through the interaction of impact cratering, fluvial erosion, and variable hydrologic forcing, *Geomorphology*, *91*, 332–363.

Howard, A., and R. Dolan (1981), Geomorphology of the Colorado River in the Grand Canyon, *J. Geol.*, *89*(3), 269–298.

Howard, A. D., and G. Kerby (1983), Channel changes in badlands, *Geol. Soc. Am. Bull.*, *94*(6), 739–752.

Howard, A. D., and J. M. Moore (2011), Late Hesperian to early Amazonian midlatitude Martian valleys: Evidence from Newton and Gorgonum basins, *J. Geophys. Res.*, *116*, E05003, doi:10.1029/2010JE003782.

Howard, A. D., and H. E. Tierney (2011), Taking the measure of a landscape: comparing simulated and natural landscape in the Virginia Coastal Plain, USA, *Geomorphology*, *137*(1), 27–40.

Howard, A. D. et al. (1994), Modeling Fluvial Erosion on Regional to Continental Scales, *J. Geophys. Res.*, *99*(B7), 13971–13986.

Howard, A. D., et al. (2005), An intense terminal epoch of widespread fluvial activity on early Mars: 1. Valley network incision and associated deposits, *J. Geophys. Res.*, *110*, D12S14, doi:10.1029/2005JE002459.

Hynek, B. M., and R. J. Phillips (2001), Evidence for extensive denudation of the Martian highlands, *Geology*, *29*(5), 407–410.
Hynek, B. M., and R. J. Phillips (2003), New data reveal mature, integrated drainage systems on Mars indicative of past precipitation, *Geology*, *31*(9), 757–760.
Hynek, B. M., et al. (2010), Updated global map of Martian valley networks and implications for climate and hydrologic processes, *J. Geophys. Res.*, *115*, E09008, doi:10.1029/2009JE003548.
Irwin, R. P., III et al. (2002), A large lake basin at the head of Ma'adim Vallis, Mars, *Science*, *296*(21 June 2002), 2209–2212.
Irwin, R. P. I., et al. (2004), Geomorphology of Ma'adim Vallis, Mars, and associated paleolake basins, *J. Geophys. Res.*, *109*, E12009, doi:10.1029/2004JE002287.
Irwin, R. P., III et al. (2005a), Interior channels in Martian valley networks: Discharge and runoff production, *Geology*, *33*(6), 489–492.
Irwin, R. P., III, et al. (2005b), An intense terminal epoch of widespread fluvial activity on early Mars: 2. Increased runoff and paleolake development, *J. Geophys. Res.*, *110*, E12S15, doi:10.1029/2005JE002460.
Irwin, R. P., III, et al. (2008), Fluvial valley networks on Mars, in *River Confluences, Tributaries and the Fluvial Network*, edited by S. P. Rice, et al., pp. 419–450, John Wiley & Sons, Chichester.
Irwin, R. P., III, et al. (2011), Topographic influences on development of Martian valley networks, *J. Geophys. Res.*, *116*, E02005, doi:10.1029/2010JE003620.
Jaumann, R., et al. (2005), Interior channels in Martian valleys: Constraints on fluvial erosion by measurements of the Mars Express High Resolution Stereo Camera, *Geophys. Res. Lett.*, *32*, L16203, doi:10.1029/2005GL023415.
Jaumann, R. et al. (2008), Fluvial erosion and post-erosional processes on Titan, *Icarus*, *197*, 526–538.
Jerolmack, D. J., et al. (2004), A minimum time for formation of Holden Northeast fan, Mars, *Geophys. Res. Lett.*, *31*, L21701, doi:10.1029/2004GL021326.
Kereszturi, A. (2005), Cross-sectional and longitudinal profiles of valleys and channels in Xanthe Terra on Mars, *J. Geophys. Res.*, *110*, E12S17, doi:10.1029/2005JE002454.
Kessler, A., and M. H. Diskin (1991), The efficiency function of detention reservoirs in urban drainage systems, *Water Resour. Res.*, *27*(3), 253–258.
Kite, E. S., et al. (2011), Chaos terrain, storms, and past climate on Mars, *J. Geophys. Res.*, *116*, E10002, doi:10.1029/2010JE003792.
Kite, E. S., et al. (2013), Seasonal melting and the formation of sedimentary rocks on Mars, with predictions for the Gale Crater mound, *Icarus*, *223*, 181–210.
Knighton, A. D. (1987), River channel adjustment The downstream dimension, in *River Channels*, edited by K. S. Richards, pp. 95–128, Basil Blackwell, Oxford.
Laskar, J. et al. (2004), Long term evolution and chaotic diffusion of the insolation quantities of Mars, *Icarus*, *170*, 343–364.
Leopold, L. B., and T. J. Maddock (1953), The hydraulic geometry of stream channels and some physiographic implications, 1–53 pp, U.S. Geological Survey.
Luo, W., and T. F. Stepinski (2009), Computer-generated global map of valley networks on Mars, *J. Geophys. Res.*, *114*, E11010, doi:10.1029/2009JE003357.
Malin, M. C., and K. S. Edgett (2003), Evidence for persistent flow and aqueous sedimentation on early Mars, *Science*, *302*, 1931–1934.
Matsubara, Y., and A. D. Howard (2009), A spatially-explicit model of runoff, evaporation and lake extent: Application to modern and late Pleistocene lakes in the Great Basin region, western United States, *Water Resour. Res.*, *45*, W06425, doi:10.1029/2007WR005953.
Matsubara, Y., et al. (2011), Hydrology of early Mars: Lake Basins, *J. Geophys. Res.*, *116*, E04001, doi:10.1029/2010JE003739.
McEnroe, B. M. (1992), Preliminary sizing of detention reservoirs to reduce peak discharges, *J. Hydraul. Eng. ASCE*, *118*(11), 1540–1549.
Melosh, H. J. (1989), *Impact Cratering, a Geologic Process*, Oxford University Press, Oxford, pp. 245 .
Milly, P. C. D. (1994), Climate, soil water storage, and the average annual water balance, *Water Resour. Res.*, *30*, 2143–2156.
Miotto, F., et al. (2007), An analytical index for flood attenuation due to reservoirs, in *32nd Congress of IAHR*, edited, Venice, Italy.
Moore, J. M., and A. D. Howard (2005), Large alluvial fans on Mars, *J. Geophys. Res.*, *110*, E04005, doi:10.1029/2004JE002352.
Moore, J. M., et al. (2003), Martian layered fluvial deposits: Implications for Noachian climate scenarios, *Geophys. Res. Lett.*, *30*(24), 2292, doi:10.1029/2003GL019002.
Oviatt, C. G. (1997), Lake Bonneville fluctulations and global climate change, *Geology*, *25*(2), 155–158.
Penido, J. C. et al. (2013), Scaling relationships and concavity of small valley networks on Mars, *Planet. Space Sci.*, *75*, 105–116.
Pizzuto, J. E. (1992), The Morphology of Graded Gravel Rivers - a Network Perspective, *Geomorphology*, *5*(3–5), 457–474.
Scanlon, K. E., et al. (2012), Orographic precipotation on early Mars: Towards new climate constraints, paper presented at Third Conference on Early Mars, Lake Tahoe, Nevada, May 21–25, 2012.
Segura, T. L. et al. (2012), An impact-induced, stable, runaway climate on Mars, *Icarus*, *220*, 144–148.
Sklar, L. S., and W. E. Dietrich (2001), Sediment and rock strength controls on river incision into bedrock, *Geology*, *29*(12), 1087–1090.
Sklar, L. S., and W. E. Dietrich (2004a), River incision into bedrock by saltating bedload I: Development of a mechanistic model, *Water Resour. Res.*, in press.
Sklar, L. S., and W. E. Dietrich (2004b), A mechanistic model for river incision into bedrock by saltating bed load, *Water Resour. Res.*, *40*, W06301, doi:10.1029/2003WR002496.
Sklar, L. S., and W. E. Dietrich (2006), The role of sediment in controlling steady-state bedrock channel slope: Implications of the saltation–abrasion incision model, *Geomorphology*, *82*, 58–83.
Whipple, K. X., and G. E. Tucker (1999), Dynamics of the stream-power river incision model: Implications for height limits of mountain ranges, landscape response timescales, and research needs, *J. Geophys. Res.*, *104*(B8), 17661–17674.
Whipple, K. X., and G. E. Tucker (2002), Implications of sediment-flux-dependent river incision models for landscape evolution, *J. Geophys. Res.*, *107*, 2039, doi:10.1029/2000JB000044.
Wordsworth, R., et al. (2011), Comparison of scenarios for Martian valley network formation using a 3D model of the early climate and water cycle, paper presented at EPSC-DPS Joint Meeting, Nantes, France.
Wordsworth, R. et al. (2013), Global modelling of the early martian climate under a denser CO2 atmosphere: Water cycle and ice evolution, *Icarus*, 1–19.